

*Digital Comprehensive Summaries of Uppsala Dissertations
from the Faculty of Science and Technology 2491*

Analysis of neutron cameras and spectrometers with digital data acquisition at tokamaks

LINUS HÄGG



ACTA UNIVERSITATIS
UPSALIENSIS
2025

ISSN 1651-6214
ISBN 978-91-513-2348-0
urn:nbn:se:uu:diva-545704



UPPSALA
UNIVERSITET

Dissertation presented at Uppsala University to be publicly examined in Högssalen, Ångströmlaboratoriet, Lägerhyddsvägen 1, Uppsala, Friday, 21 February 2025 at 08:00 for the degree of Doctor of Philosophy. The examination will be conducted in English. Faculty examiner: Professor Andreas Zimbal (Physikalisch-Technische Bundesanstalt).

Abstract

Hägg, L. 2025. Analysis of neutron cameras and spectrometers with digital data acquisition at tokamaks. *Digital Comprehensive Summaries of Uppsala Dissertations from the Faculty of Science and Technology* 2491. 72 pp. Uppsala. ISBN 978-91-513-2348-0.

The neutron emission from a fusion plasma can be measured with neutron diagnostics and analysed to estimate plasma quantities. This thesis covers the subject of neutron detection methods using scintillators. It follows the detection process from the scintillation phenomenon and the hardware solutions in the data acquisition, to the software data handling and pulse analysis in the data reduction. It also covers the relationship between the measured scintillation light pulse to the incident neutron energy, using light yield calibration methods and system response functions. In particular, this thesis has focused on the development of methods and codes that allows us to exploit the possibilities offered by fully digital data acquisition systems.

In the latter half of the thesis, these methods are put into practice for two neutron diagnostic systems at JET, the neutron camera and the MPRu neutron spectrometer. The neutron camera is used to estimate the estimate the volume integrated neutron yield. The method was developed in two iterations, and was applied to measurement data from recent JET DD and DT experiment campaigns. In its latest iteration, the method absolutely calibrates the neutron camera. Comparisons with neutron yield estimates from the JET fission chambers reveal inconsistencies between the two instruments, and between the two iterations of the method for the neutron camera. These discoveries prompt further investigation into the method.

For the MPRu, a framework was developed for estimating two fusion plasma quantities; the plasma rotation and the thermonuclear emission. The line of sight for the MPRu is advantageous for evaluating these quantities in the core of the plasma. The framework shows great promise, and has the potential of providing complementary measurements to diagnostics which have trouble penetrating into the core.

The techniques developed in this work can be refined for their current use, and may also be adapted for other similar neutron diagnostic systems.

Keywords: Neutrons, neutron diagnostics, scintillators, data acquisition, data reduction, JET, fusion plasma, neutron yield, plasma rotation, thermonuclear emission, JET neutron camera, MPRu

Linus Hägg, Department of Physics and Astronomy, Applied Nuclear Physics, Box 516, Uppsala University, SE-751 20 Uppsala, Sweden.

© Linus Hägg 2025

ISSN 1651-6214

ISBN 978-91-513-2348-0

URN urn:nbn:se:uu:diva-545704 (<http://urn.kb.se/resolve?urn=urn:nbn:se:uu:diva-545704>)

Till Birgitta, Christer, Annie, och Alice

List of Papers

This thesis is based on the following papers, which are referred to in the text by their Roman numerals.

- I. Hägg, L., Binda, F., Conroy, S., Ericsson, G., Ghani, Z., Giacomelli, L., Marocco, D., Milocco, A., Riva, M., Andersson Sundén, E., and JET Contributors (2023) **Estimating the neutron yield in a deuterium plasma with the JET neutron camera.** *Review of Scientific Instruments*, 94, 073502
- II. Hägg, L., Conroy, S., Ericsson, G., Ghani, Z., Giacomelli, L., Marocco, D., Milocco, A., Riva, M., Eriksson, B., Robertson, G., Eriksson, J., Andersson Sundén, E., JET Contributors, and The Eurofusion Tokamak Exploitation Team (2024) **Estimating the neutron yield in a deuterium-tritium plasma with the JET neutron camera.** *Review of Scientific instruments* (submitted)
- III. Hägg, L., Eriksson J., Conroy, S., Ericsson, G., Kirov, K., Andersson Sundén, E., and JET Contributors (2024) **Plasma rotation and thermonuclear neutron emission estimates in JET deuterium-tritium plasmas from neutron spectroscopy.** *Plasma Physics and Controlled Fusion* (submitted)

Reprints were made with permission from the respective publishers.

Cover page:

An elusive detector box from the JET neutron camera

By Linus Hägg

Contents

1. Introduction.....	11
1.1 Fusion Reactions	11
1.2 Magnetic Confinement.....	13
1.2.1 External Heating	14
1.3 Fusion Plasma Quantities	15
1.4 Aim of the Thesis	15
2. Neutron Detection	16
2.1 Data Acquisition.....	16
2.1.1 Scintillators	16
2.1.2 Photomultipliers.....	17
2.2 Data Reduction.....	18
2.2.1 Data Records.....	18
2.2.2 Pulse Height Spectrum	19
2.2.3 Pulse Shape Discrimination.....	20
2.2.4 Pile-Up.....	22
2.3 Light Yield Calibration	24
2.3.1 Electron Equivalent Energy	24
2.3.2 Light Yield Spectrum	24
2.3.3 Gamma Calibration.....	25
2.3.4 Thermal Calibration.....	27
2.3.5 Light Yield Functions	28
2.4 System Response Matrix.....	30
2.4.1 Definitions	30
2.4.2 Examples	30
2.4.2 Light Yield Thresholds	32
2.5 Measurement Techniques.....	32
2.5.1 Proton Recoil Scintillators.....	32
2.5.2 Thin-Foil Proton Recoil.....	33
2.5.3 Fission Chambers.....	33
3. The JET Neutron Camera	34
3.1 Instrument.....	34
3.2 Data Reduction Specifics	36
3.2.1 Dynamic Record Lengths	36
3.2.2 Pile-Up Treatment	37
3.3.3 Gamma Discrimination.....	37

3.3 Measurement Data.....	38
3.4 Models and Simulations.....	39
3.4.1 Neutron Emissivity Profiles.....	40
3.4.2 Neutron Energies.....	41
3.4.3 LINE2.1.....	43
3.4.4 System Response.....	44
3.4.5 Backscatter.....	45
3.4.6 Neutron Emissivity Profile Fit.....	45
3.5 Neutron Yield Estimates.....	46
3.6 Reflections on Papers I and II.....	49
3.6.1 Inconsistencies.....	49
3.6.2 Challenges.....	49
4. The MPRu.....	50
4.1 Instrument.....	50
4.2 Measurement Data.....	51
4.3 Data Reduction Exploration.....	54
4.3.1 LED Removal.....	54
4.3.2 Escape Event Correction.....	56
4.4 Modelling and Analysis.....	58
4.4.1 Neutron Spectrum Modelling.....	59
4.4.2 Neutron Spectrum Fit.....	60
4.5 Results.....	61
4.5.1 Plasma Rotation.....	61
4.5.2 Thermonuclear Emission.....	62
4.6 Reflections on Paper III.....	63
4.6.1 Charge Exchange Comparison.....	63
4.6.2 Data Reduction.....	63
4.6.3 Outlook.....	63
5. Conclusions.....	65
6. Summary in Swedish.....	66
7. Acknowledgements.....	68
Bibliography.....	69

Abbreviations

ADC	Analogue to Digital Converter
DAQ	Data Acquisition
D	Deuterium
DD	Deuterium-Deuterium
DT	Deuterium-Tritium
FWHM	Full Width Half Maximum
ITER	International Thermonuclear Test Reactor
JET	Joint European Torus
LOS	Line of Sight
MCNP	Monte Carlo N-Particle transport code
MPRu	Upgraded Magnetic Proton Recoil Spectrometer
NBI	Neutral Beam Injection
PHS	Pulse Height Spectrum
PMT	Photomultiplier Tube
PSD	Pulse Shape Discrimination
RF	Radio-Frequency
T	Tritium

1. Introduction

Nuclear fusion as an energy source is an increasingly interesting prospect in the current global landscape of energy insecurities and climate change. The concept has always shown incredible potential, but the path towards fusion energy is not without its challenges. The work to realize this energy source spans decades. It has brought about large multi-national collaborations and experiments, such as the highly influential Joint European Torus (JET) and the awe-inspiring megaproject that is ITER.

1.1 Fusion Reactions

Fusion experiments use light nuclei, such as deuterium (D) and tritium (T), to fuel fusion reactions. A set of relevant reactions for such fuel is shown in Table 1, along with their respective branching ratios β , Q-values, and neutron energies E_N (where applicable). In this thesis, reactions #1 and #4 are referred to as the DD and DT reactions, and their respective neutrons as DD and DT neutrons.

In terms of fuel availability, deuterium is very abundant since it can be extracted from seawater. ^3He is found naturally in very small quantities on earth, and sourcing it from deposits on the moon is still a far-fetched idea. Tritium is not abundant either, and it is a radioactive hydrogen isotope with a half-life of 12 years. However, there are means and methods for producing tritium to fuel future fusion reactors. One such method proposes a tritium breeding blanket in the reactor wall. Fusion neutrons are absorbed in lithium in the blanket, which produces tritium according to the $^6\text{Li}(n,T)^4\text{He}$ reaction.

Among the reactions in Table 1, the DT reaction is the most suitable for high power fusion experiments. This is based on its high Q-value and its high reactivity at a given temperature. The fuel reactivity $\langle\sigma v\rangle_{i,j}$ between reactant species i and j is given by

$$\langle\sigma v\rangle_{i,j} = \iint f_i(v_i)f_j(v_j)\sigma(|v_i - v_j|)|v_i - v_j|d^3v_id^3v_j \quad (1.1)$$

where v_i and v_j are the reactant velocities, $f_i(v_i)$ and $f_j(v_j)$ are the reactant velocity distributions, and $\sigma(|v_i - v_j|)$ is the reaction cross section as a function of the relative velocity.

In fusion research, the temperature is often given in the energy unit electronvolts (eV). This is a simple conversion using Boltzmann's constant, where 300 K corresponds to 0.026 eV.

If the ions are in a thermal equilibrium, their distributions are described by a Maxwellian, which only depends on the fuel temperature. Consequently, the resulting reactivities will also be a function of temperature. This thermal reactivity for each of the reactions is found in Figure 1.

Table 1: Important fusion reactions, their branching ratios β , the Q-values, and the neutron energy E_N for reactions #1 and #4.

#	Reaction	β	Q [MeV]	E_N [MeV]
1	$D + D \rightarrow n + {}^3\text{He}$	0.5	3.3	2.45
2	$D + D \rightarrow p + T$	0.5	4.0	-
3	$D + {}^3\text{He} \rightarrow p + {}^4\text{He}$	1	18.4	-
4	$D + T \rightarrow n + {}^4\text{He}$	1	17.6	14.0

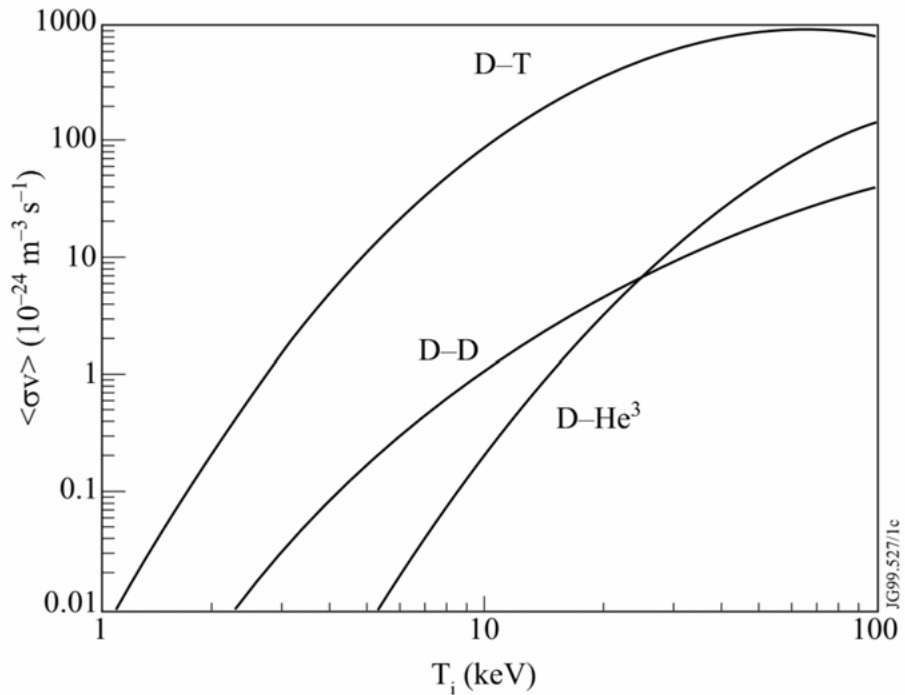


Figure 1: Thermal reactivities as a function of reactant temperature for the fusion reactions from Table 1, combined for reaction #1 and #2. Reference number JG99.527/1c in the JET Figure Database [43], Copyright by EFDA-JET.

The fusion power P_{fusion} is given by an integral over the plasma volume V_{plasma} as

$$P_{fusion} = \int_{V_{plasma}} \frac{n_i n_j}{1 + \delta_{i,j}} \langle \sigma v \rangle_{i,j} Q_{i,j} dV \quad (1.2)$$

where n_i and n_j are the reactant densities, $Q_{i,j}$ is the Q-value for the reaction, and $\delta_{i,j}$ is the Kronecker delta function to avoid double counting if $i = j$. Here it is doubly apparent that the DT reaction is an excellent candidate, thanks to its high reactivity and high Q-value.

For the high temperatures where the reactivities are also high in Figure 1, the fuel reactants are in a plasma state, where the reactants are fully ionized and intermixed with the electrons. Reaching the higher reactivities, and therefore the higher fusion powers, necessitates some form of heating of the fusion plasma. The DT reaction produces both a 14 MeV neutron, which escapes the plasma because of its neutral charge, and a 3.5 MeV α -particle. The latter can deposit its energy through collisions with the ions and electrons in the plasma, this is known as α -particle heating. In order to fully utilize this internal heating and apply further external heating, the plasma must be confined in some way.

1.2 Magnetic Confinement

Magnetic confinement is a technique used to confine a fusion plasma in a vacuum vessel using magnetic fields. As the charged particles of the plasma move in a magnetic field, they are subject to the Lorentz force. The equation of motion for a charged particle with the velocity \mathbf{v} , charge q , and mass m , is then described by

$$\frac{d\mathbf{v}}{dt} = \frac{q}{m} (\mathbf{v} \times \mathbf{B}) \quad (1.3)$$

for the magnetic flux density \mathbf{B} . The acceleration is perpendicular to the magnetic field and the velocity, confining the particle to gyrate around the magnetic field lines with the cyclotron frequency

$$\omega_c = \frac{qB}{m}. \quad (1.4)$$

The confinement can then be completed if the magnetic field lines are closed in a circular shape, forming a torus for a larger plasma volume. This is used in tokamak reactors configurations [1], see Figure 2. Toroidal field coils around the torus generate a toroidal magnetic field, and an induced toroidal current generates a poloidal field. The resulting field affecting the plasma is a helical magnetic field, which twist around the torus. Additional reading on this subject can be found in [2].

Some of the largest tokamak devices that have been constructed so far JET [3] in the UK, TFTR [4] in the USA, and JT60 [5] in Japan. The largest yet will be ITER [6], which is currently being built in France.

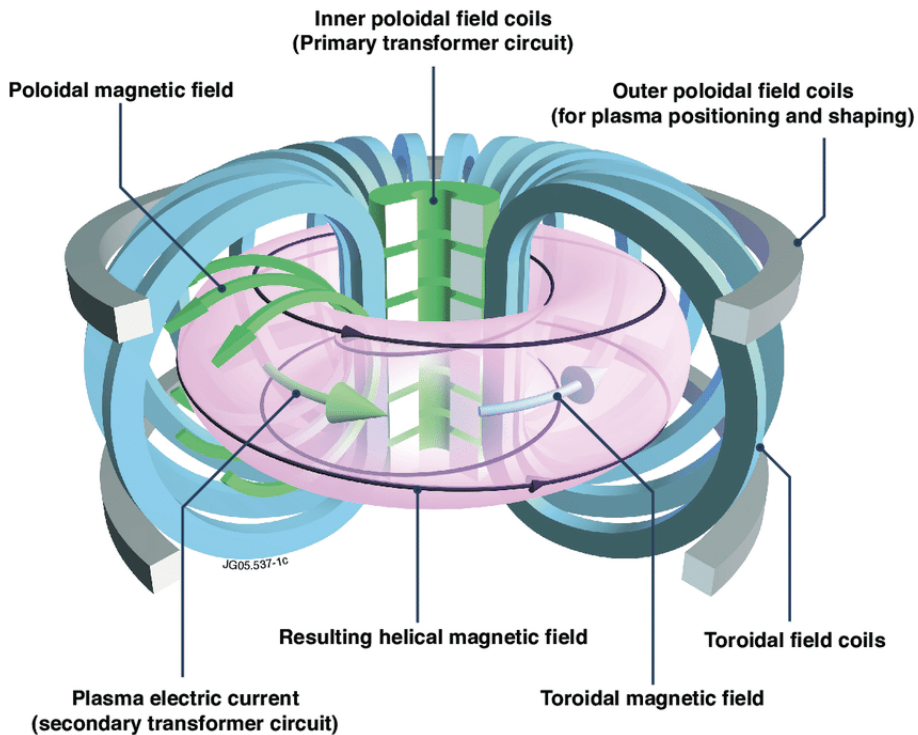


Figure 2: Illustration of a tokamak concept, the toroidal plasma current, and the magnetic field components. Reference number JG05.537-1c in the JET Figure Database [43], Copyright by EFDA-JET.

1.2.1 External Heating

The fusion plasma in a tokamak can be heated by external sources, in addition to the internal heating by α -particles. The three main heating systems used in fusion experiments are Ohmic heating, neutral beam injection (NBI), and radio frequency heating (RF). The RF heating can be performed with different techniques, here we only discuss ion cyclotron resonance heating (ICRH).

For Ohmic heating, the plasma is heated through resistivity, in response to the toroidal current. For increased electron temperatures, this resistivity decreases. As a result, Ohmic heating is not sufficient to heat the plasma for high power experiments.

An NBI system uses a particle accelerator to inject D and/or T atoms, which both fuels and heats the plasma. The beam atoms quickly ionize, and the resulting ions deposit their energy through collisions with ions and electrons in the bulk plasma. At JET, the beam energies are typically around 100 keV.

ICRH systems generate high frequency electromagnetic waves from antennas facing the plasma. The frequencies of the waves are chosen to match the cyclotron frequency (see Equation 1.4) of specific plasma ions, to transfer power to a specific location in the plasma.

Additional reading on this subject can be found in [7].

1.3 Fusion Plasma Quantities

Fusion experiments devices have many types of detector systems for measuring various plasma quantities. This thesis primarily looks at three specific quantities; the volume integrated neutron yield, the thermonuclear emission, and the plasma rotation.

The volume integrated neutron yield is directly related to the fusion power of the plasma, since, e.g., one DT neutron indicates that one DT reaction took place. At JET, the neutron yield is typically monitored with fission chambers, see section 2.5.3 Fission Chambers. In Paper I and II, the integrated neutron yield is estimated using the JET neutron camera.

The thermonuclear emission is here defined as neutron emissions from fusion reactions in the thermal bulk plasma, i.e. the sub-population of plasma ions that have a Maxwellian energy distribution. This emission is quantified with respect to emission from fusion reactions involving supra-thermal ions, meaning those heated by NBI or RF. In Paper III, the thermonuclear emission is estimated using the MPRu neutron spectrometer at JET.

The plasma rotation, in this context, refers to the toroidal velocity of the thermal bulk plasma [8]. There is a small amount of spontaneous plasma rotation [9], but significant plasma rotation is induced from the momentum injected by the NBI. This rotation gives rise to a Doppler-shift of the energy spectrum of emitted particles. In Paper III, the plasma rotation is estimated using the MPRu neutron spectrometer at JET.

1.4 Aim of the Thesis

This thesis focuses on methods and codes for utilizing full digital data acquisition systems, which have been installed on both the JET neutron camera and the MPRu neutron spectrometer in recent years. A digital data acquisition system enables detailed analysis of the measurement data. This allows us to draw more conclusions regarding individual particle interactions in the detection systems. These methods include features such as pulse shape analysis (section 2.2 Data Reduction) and light yield calibration (section 2.3 Light Yield Calibration). In this thesis, we show how to use digital data acquisition systems to perform data reduction and calibration, for an improved analysis of recent JET data.

2. Neutron Detection

One of the key challenges of neutron detection lies in the neutral electric charge of the particle. Detection methods of neutron energies must often rely on indirect measurements, through the detection of secondary particles or light emission originating from a neutron interaction. This also comes with complications in relating these second-hand measurements to the incident neutron energy. This part of the thesis covers neutron detection methods using scintillators, and data reduction techniques used to analyse such measurements.

2.1 Data Acquisition

2.1.1 Scintillators

A scintillating material generates a light pulse in response to excitations, such as when a charged particle interacts with the material. The light pulse can be used to indicate the particle's presence, and the number of photons is proportional to the deposited energy. Scintillator detectors make use of this phenomenon to either detect charged particles directly, or to detect neutral particles through secondary charged particles. Neutrons and gammas are detected through their interactions with protons and electrons in the material, respectively.

The most common scintillator materials are either of the inorganic or organic type. Inorganic scintillators typically have a higher light output but a slower response time, compared to organic scintillators [10]. In this thesis, we focus on organic scintillators of hydrogen- and carbon-rich materials. The high hydrogen content makes them well suited for neutron detection, as it facilitates high energy deposition from elastically scattering neutrons. The works in Papers I, II, and III all use organic scintillators.

In Paper I, NE213 liquid scintillators [11] are used in the JET neutron camera to detect DD neutrons. In some organic scintillators, such as NE213, the type of particle inducing excitations affects the shape of the light pulse. The excitations will contain a certain amount of long-lived triplet states, leading to a delayed component in the light pulse. This component is stronger for ionizing particles with a high rate of energy loss. As a result, protons will give rise to a larger delayed component compared to electrons [10]. This allows us to

distinguish between neutron-induced and gamma-induced events with a pulse shape discrimination method, see section 2.2.3 Pulse Shape Discrimination.

In Paper II, BC418 plastic scintillators [12] are used in the JET neutron camera to detect DT neutrons. The relatively short light pulse decay time of a BC418 scintillator, compared to NE213, makes it well suited for high count rate experiments, such as DT plasmas at JET. The small size of these specific BC418 scintillators also allow for mechanical gamma discrimination, where highly energetic gammas are very likely to pass through the detector without depositing any energy.

In Paper III, phoswich scintillators [10] are used in the MPRu to detect protons (see section 2.5.2 Thin-Foil Proton Recoil). A phoswich scintillator has two layers of different scintillating materials, with dissimilar light pulse decay times. Particles that arrive from a specific direction and manage to deposit energy in both layers will generate a light pulse of a characteristic shape, which aids background discrimination.

2.1.2 Photomultipliers

The light output from a single scintillation light pulse is weak, which necessitates some kind of amplification to create a usable signal. This is often accomplished using a photomultiplier tube (PMT), though there are alternative light detectors, such as semiconductor photodiodes, that can fulfil the same purpose [10] [13].

Many commercial scintillator detectors have a built-in photomultiplier tube, an example illustration of such a design is found in Figure 3. In this design, the scintillating material housed in a reflecting casing. One side of the casing is open to a lightguide (usually of plastic or glass) leading to the PMT.

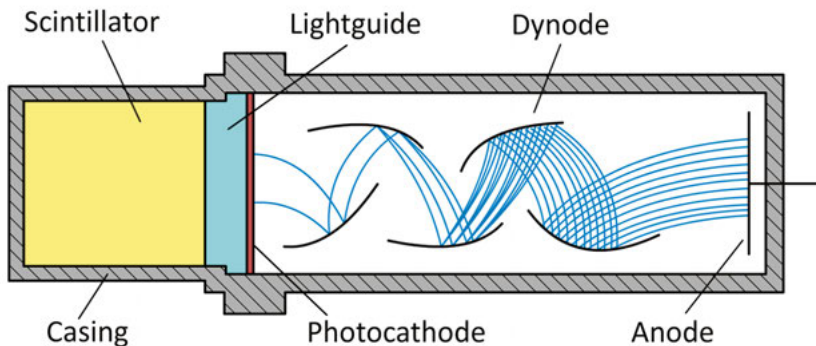


Figure 3: Illustrated design of a scintillator detector with a built-in photomultiplier tube.

The main components of a PMT are a photocathode and an electron multiplier structure, both of which are encased in a vacuum tube. The photocathode converts incident photons to low-energy electrons, utilizing the photoelectric

effect. An electric field in the vacuum tube accelerates these photoelectrons towards a series of dynodes. When a dynode is struck by an energetic photoelectron, the excitation results in the emission of more than one electron, which are in turn accelerated towards the next dynode. After the series of dynodes, the amplified charge is collected at the anode [10].

A typical scintillation light pulse may only produce a few hundred photoelectrons at the photocathode. These are multiplied to a sufficient magnitude, and the resulting electrical signal will be a pulse of a similar time duration as the incident light pulse. In the data acquisition (DAQ) systems used in this thesis, the PMT signal is then fed to a digitizer which converts it into discrete voltage measurements (samples). Each scintillation event is then analysed in the data reduction codes.

It is also possible to process the PMT signals with a single analog-to-digital converter (ADC), where just the pulse height is saved as a digital value. While these devices still have their niche, saving the full pulse shape allows for a more detailed off-line analysis.

2.2 Data Reduction

2.2.1 Data Records

PMT signals are fed through a digitizer, which samples the voltage levels of the signal according to its sampling frequency. When a sample exceeds the digitizer's set trigger level, the signal is saved as a data record containing a set number of samples, the record length. Most devices can also set pre-trigger samples, where a number of samples before the triggering pulse are saved at the start of the record. This allows the baseline to be analysed for each event. A record with an example pulse from Paper III can be seen in Figure 4.

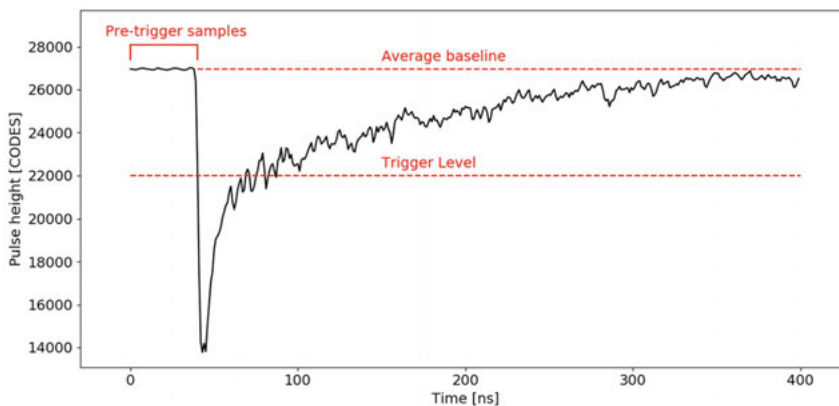


Figure 4: Example data record from the MPRu, Paper III. Marked in red is the region of pre-trigger samples, the average baseline, and the trigger level.

Some digitizers are equipped with advanced features such as real-time pulse detection and noise correction [14], which can be valuable in a system designed for fast analysis or even live-feedback. However, if time and storage space permits, there is merit in avoiding such features to preserve the raw data as far as possible. Similar pulse-identification techniques could always be used later in the data reduction process in a reversible manner.

With a set record length and a set pre-trigger length, it is usually trivial to find and process the pulse in each record. The data reduction code can also utilize vectorization to expediently process large amounts of data. However, there are situations with additional complications, see section 2.2.4 Pile-Up.

2.2.2 Pulse Height Spectrum

Each data record is processed by quantifying either the pulse height or the area under the pulse. Both of these quantities can be used as a measure of the light yield from a specific scintillator event. The pulse area is often preferred since it contains information about the original scintillator light pulse shape, this is explored further in section 2.2.3 Pulse Shape Discrimination. The pulse area is presented in units of codes, the digitizer's discrete scale for voltage measurements. The works presented in Papers I, II, and II all use pulse areas to quantify the collected light.

Prior to integrating over the pulse - to extract the pulse area - a baseline subtraction is often performed. The average background, as estimated from the pre-trigger samples, is subtracted from the entire record. This is to make pulse areas comparable even if the baseline drifts between different values over time. There are more complicating cases, such as when the baseline oscillates fast enough to vary significantly within individual records. In these scenarios, a dedicated baseline restoration method is warranted, as used in [15], rather than a simple baseline subtraction.

Once all records over a measurement period are processed, the result can be histogrammed in a so-called pulse height spectrum (PHS). For traditional reasons, this name is often used even if the histogram displays the pulse area, rather than the pulse height. An example of a PHS from Paper II is found in Figure 5. The PHS is a light yield spectrum, rather than a direct energy measurement. The relation between light yield, the deposited energy, and the full energy of the incident particle is detailed in sections 2.3 Light Yield Calibration and 2.4 System Response Matrix.

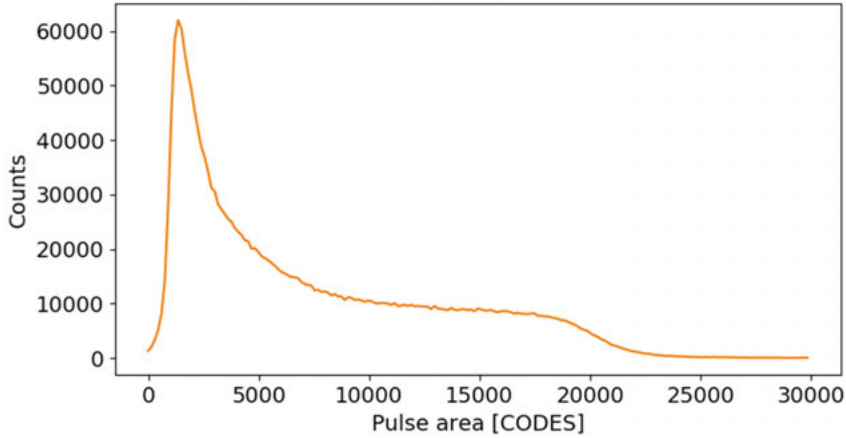


Figure 5: Pulse height spectrum from the JET neutron camera, Paper II.

2.2.3 Pulse Shape Discrimination

When the shape of a scintillator light pulse holds relevant information, a pulse shape discrimination method can be used to classify different types of events or reveal specific features of a measurement. This involves setting two or more integration intervals, also called gates, to compare different parts of a pulse. The pulse area within each gate can then be plotted in a multidimensional histogram, typically just a 2D histogram for two gates. This method is used in slightly different ways in Papers I, II, and III, where different detector types are used.

For example, the NE213 scintillator can detect both neutrons and gammas, but neutron-induced light pulses have a longer decay time than gamma-induced events (as discussed in section 2.1.1 Scintillators). A shorter gate can cover the peak of the pulse while a longer gate covers its delayed component. In Figure 6 is a showcase of these kinds of gates applied to two pulse shapes, identified as a neutron-induced and a gamma-induced event. This scenario is from Paper I, where the two pulse areas are defined as Q_S and Q_L for the short- and long gate respectively. The integral over the full pulse shape is also recorded as Q_{TOT} . The two events in Figure 6 have equivalent Q_{TOT} values, meaning that it is only their pulse shape that differentiates them.

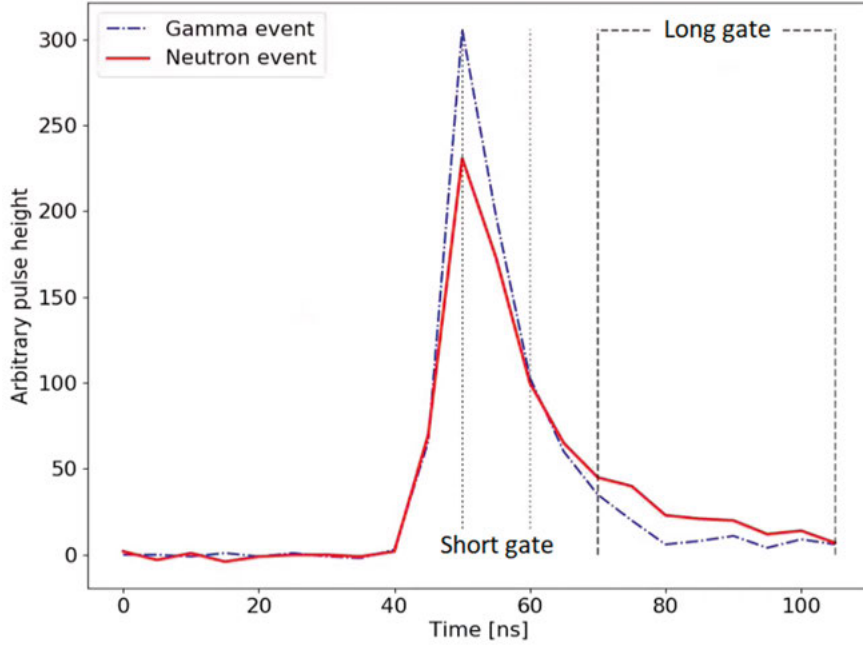


Figure 6: Two data records from the JET neutron camera, in Paper II. The events are identified as a gamma-induced event and a neutron-induced event. The boundaries of each gate are shown as vertical dashed and dotted lines.

In Figure 7 is a 2D histogram from Paper 1, using the aforementioned gates. On the x-axis is Q_{TOT} while the ratio Q_S/Q_L is on the y-axis. As can be seen in Figure 6, neutron events are expected to have a larger deposition in the long gate. This leads to a larger Q_L value, and consequently a smaller Q_S/Q_L ratio. This PSD method has separated neutron- and gamma-induced events vertically, where the lower cluster consists of neutron-induced events. The two groups are separated through a PSD selection, as shown by the dark line in Figure 7.

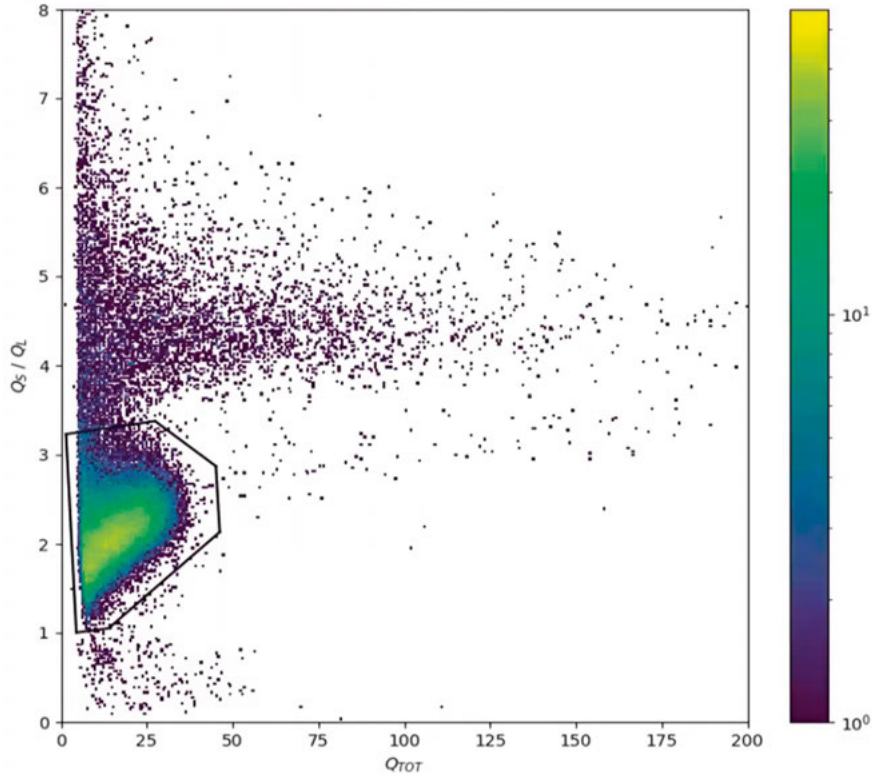


Figure 7: PSD 2D histogram for the JET neutron camera, Paper I, detector channel 15. The dark line around the lower cluster marks the PSD selection. Events within the selection are identified as neutron-induced events.

Finding which gates yield the best separation between two types of events is often an optimization problem. The gate settings can be found in a fit that minimizes a figure of merit. The fit could either process averaged representatives of each event type, a larger dataset of each type, or a fit representing the distribution of each type, as is done in [16].

2.2.4 Pile-Up

In a high rate measurement, multiple particles can give rise to a signal in the detector close together in time, leading to their PMT signals ending up in the same data record. This phenomenon is referred to as pile-up. Depending on how close the two pulses are, one may only be partially recorded in the record, or the two pulses may fully or partially overlap, see Figure 8. Either case leads to deceptively large pulse areas for some pile-up events. In a PSD method (see section 2.2.3 Pulse Shape Discrimination), a partial overlap may only inflate the pulse area in one of the gates, resulting in a misleading pulse shape analysis.

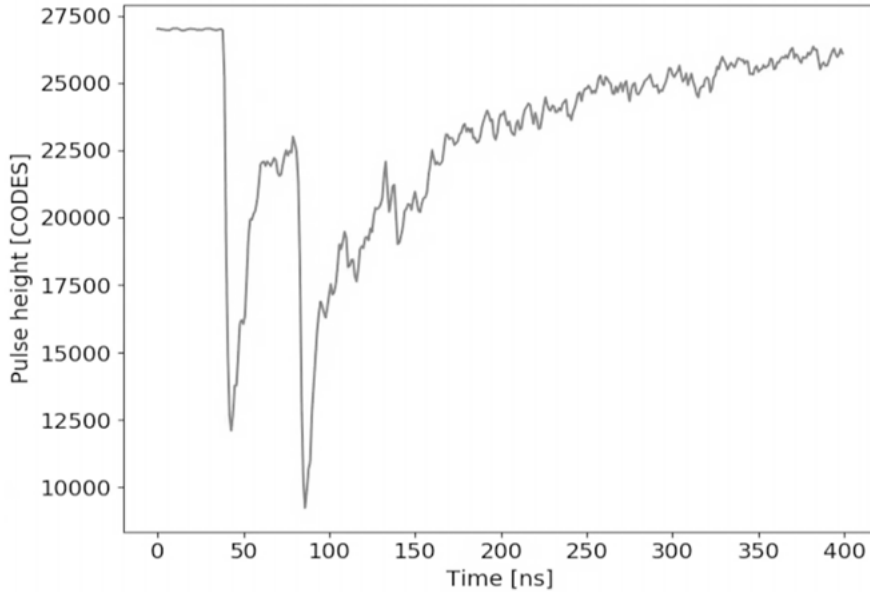


Figure 8: Example data record from the MPRu, Paper III, with a pile-up event.

Pile-up events are usually found through some sort of peak-identification code, such as the function `find_peaks` from the SciPy library of the Python programming language [17]. Records that contain two or more prominent peaks can be classified as a pile-up event. If the pulses do not overlap, they can be individually treated as normal events. In cases where they do overlap, one must either estimate the impact of pile-up events (as is done in Paper II) or use a pile-up reconstruction algorithm [18] to restore pulses that overlap. It is also possible to leave pile-up events intact, and simulate the impact of pile-up as a component in the PHS, this is demonstrated in [19].

Pile-up can also be mitigated with the right hardware and settings in the data acquisition. The scintillator should have a short light pulse decay time to avoid closely arriving pulses from overlapping. A digitizer should have a sufficiently low dead time to avoid missing events entirely. The dead time is the period during which the digitizer cannot trigger, due to being busy with data transfers and re-arming procedures. It is also possible to partially work around pile-up by using a dynamic record length, this was utilized in [20] for the JET neutron camera. The used dynamic window data acquisition setting extends the record length when a new pulse is detected within a certain time limit. This prevents pulses being partially recorded in a pile-up record. However, the variable record lengths complicate vectorization in the data reduction code, this is addressed in section 3.2 Data Reduction Specifics.

2.3 Light Yield Calibration

The light yield from a scintillator is several steps removed from the energy of a detected neutron. A neutron can deposit any amount of its full energy in the scintillator when scattering elastically on protons in the material. The proton then induces scintillation light through its interactions when slowing down. The resulting light pulse is converted into an electrical signal in the PMT, which is often further amplified in intermediate electronics before entering the digitizer. The digitized and somewhat broadened pulse is then integrated to quantify the pulse area as a measure of the light yield. It should be clear from this overview that a calibration is needed to relate pulse area to light yield.

The unit used for scintillation light yield is eVee, which is further explained in section 2.3.1 Electron Equivalent Energy. Two light yield calibration methods are covered in this thesis. Explained in section 2.3.3 Gamma Calibration is a more general light yield calibration using a gamma source. Section 2.3.4 Thermal Calibration presents an alternative that is more specific to neutron diagnostics for fusion applications.

2.3.1 Electron Equivalent Energy

The unit eVee stands for electron equivalent energy. A light pulse with a light yield of 1 MeVee refers to the intensity of a light pulse that would be induced by an electron of 1 MeV. For most organic and many inorganic scintillators, the light yield has a linear relation to the deposited energy from an electron. For a heavier charged particle like a proton, this relationship is instead non-linear [10] [21]. Since neutrons interact with protons in a scintillator, neutron-induced events inherit this nonlinear relation between deposited energy and light yield. In the same way, gammas interact with electrons and have a linear relation instead. A gamma ray that deposits 14 MeV into a scintillator will generate a light yield of 14 MeVee by definition. The neutron nonlinearity can be described by a light yield function, see section 2.3.5 Light Yield Functions.

2.3.2 Light Yield Spectrum

The neutron's stochastic energy deposition in a scintillator gives rise to a box-like shaped PHS. In Figure 9 are several simulated pulse height spectra of a BC418 plastic scintillator resulting from a flux of monoenergetic neutrons. Aside from the exponential behaviour at the very lowest light yields, the PHS has a continuum of possible energy depositions up to a maximum value, roughly 8.9 MeVee for 14 MeV neutrons. The highest light yield corresponds to a full energy deposition by neutron. However, this does not constitute a complete light yield calibration due to the nonlinearity of neutron-induced light yields. In a real measurement, the neutron spectrum is rarely monoenergetic, and the light yield spectra in Figure 9 would also be broadened based

on the detector resolution. As a result, a modelled system response matrix is needed to relate the measured PHS to an incident neutron spectrum, though this is covered in section 2.4 System Response Matrix.

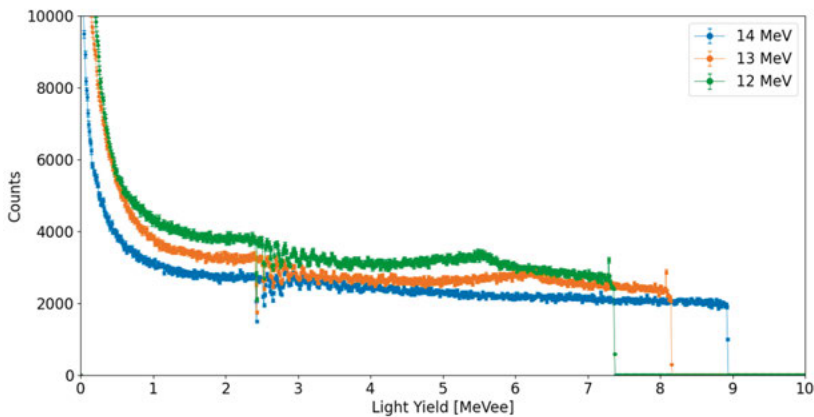


Figure 9: Several pulse height spectra for a MCNP6 (Monte Carlo N-Particle) simulation of the BC418 scintillator light yield from a flux of monoenergetic neutrons. The simulation uses the J Adams light yield function [22].

Due to the shape of the scintillator response, it is not possible to use a light yield threshold in the PHS to exclude neutrons above a certain energy. A small light yield could be the result of a small energy deposition from a neutron of any energy, as is evident in Figure 9. It is, however, possible to use a light yield threshold to exclude neutrons *below* a certain energy. A full energy deposition is related to a specific light yield, and any depositions larger than that can only originate from neutrons of a higher energy.

2.3.3 Gamma Calibration

A light yield calibration is often performed using measurements with a known gamma source, utilizing the linear relationship between energy deposition and light yield. For instance, a ^{22}Na source emits two monoenergetic gammas at 0.511 MeV and 1.275 MeV, which can be used to fix the energy scale. This method is used for the light yield calibration of the JET neutron camera in Paper I.

Gammas in these energies mainly interact via Compton scattering in the scintillator material. As a result, the scintillator response to a monoenergetic gamma is a box-like shaped PHS, very similar in shape to the response to monoenergetic neutrons Figure 9. This response can be simulated with a Monte Carlo code such as MCNP. In Figure 10 is the measured and simulated NE213 liquid scintillator response to a ^{22}Na source, from the light yield calibration in Paper I.

The detector resolution is simulated by applying a Gaussian broadening to the simulated PHS. The Gaussian broadening used in this work is defined by the full half width maximum (FWHM), applied to a specific light yield L , as

$$FWHM = a + b\sqrt{L} + cL^2 \quad (2.1)$$

where a , b , and c are resolution calibration parameters [23].

The measured PHS is expressed in MeVee by converting the pulse area measurement values Q_{TOT} to light yield L . This is done with the linear relation

$$L = k \cdot Q_{TOT} + m, \quad (2.2)$$

where k and m are calibration parameters.

The gamma light yield calibration is performed with a fit of the calibration parameters in Equations 2.1 and 2.2, which minimizes a suitable test statistic. The calibration in Paper I minimizes the CSTAT [24], which is defined as

$$CSTAT = 2 \sum_i (e_i - n_i \cdot \ln e_i) \quad (2.3)$$

where n_i are binned light yield values calculated with Equation 2.1, and e_i are binned light yield values from the simulation. An example of a completed gamma light yield calibration fit from Paper I is found in Figure 10.

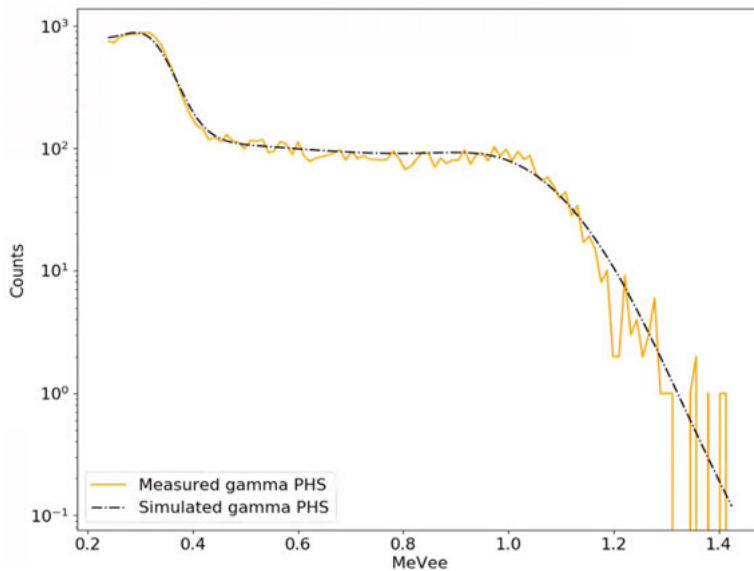


Figure 10: Pulse height spectra for a completed gamma light yield calibration, Paper I.

The ^{22}Na light yield calibration performs well in Paper I, where DD neutrons with an average energy of 2.45 MeV are measured. In Paper II, the measurements are instead of DT neutrons with an average energy of 14 MeV. Using the same kind of calibration would involve a long extrapolation to higher energies, from the relatively low gamma energies of ^{22}Na . In the absence of a suitable gamma source, so-called thermal data is instead used for a light yield calibration in Paper II.

2.3.4 Thermal Calibration

A plasma that is only subjected to Ohmic heating, i.e. without any auxiliary heating (NBI or RF), is in this thesis referred to as a pure thermal plasma. Consequently, measurement data of such a plasma is called thermal data. The neutron spectrum emitted from a thermal plasma is gaussian [25], which makes it suitable for a light yield calibration, as is done in Paper II. However, the neutron count rate from a thermal plasma is relatively low compared to that of a plasma that was heated with e.g. NBI heating. This means that thermal data must be summed over a long time period in order to perform a reliable calibration.

The thermal light yield calibration follows a similar procedure to the gamma light yield calibration. The neutron spectrum from a thermal plasma can be described as a Gaussian. The FWHM value and the central energy for this Gaussian can be calculated with the Van Belle and Sadler FPS code [26], this is detailed further in Paper II. The scintillator response is then modelled by folding the Gaussian with a system response matrix, see section 2.4 System Response Matrix. We also apply the detector resolution broadening described by Equation 2.1. This results in a simulated PHS.

The thermal data PHS is converted to MeVee using Equation 2.2. The thermal light yield calibration is completed using the same kind of CSTAT fit as described in section 2.3.3 Gamma Calibration. Though in Paper II, alternate versions of Equations 2.1 and 2.2, with fewer parameters, were used. An example of a completed thermal light yield calibration fit from Paper II is found in Figure 11.

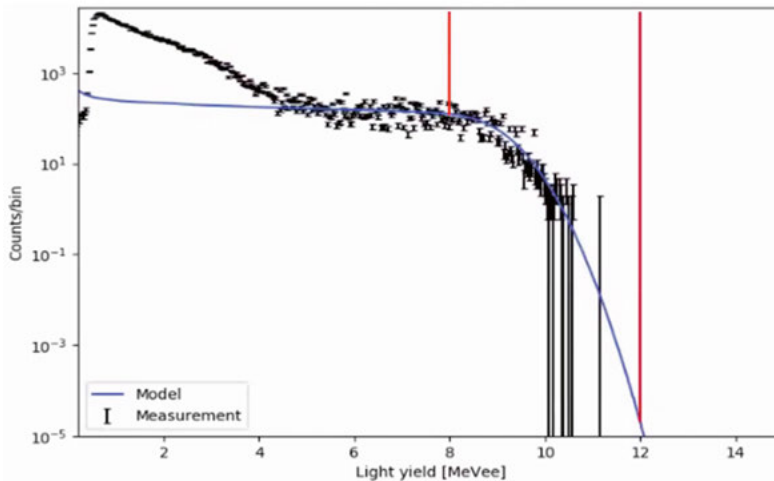


Figure 11: A completed thermal light yield calibration fit, Paper II, detector channel 15. The red vertical markers indicate the region in which CSTAT is calculated.

2.3.5 Light Yield Functions

A light yield function converts the deposited energy in units of eV, to a scintillator light yield in units of eVee. This kind of function is typically used to describe neutron energy depositions, due to their nonlinear relation to the light yield. The light yield function for a scintillator can be obtained through some method of detector characterization. Either with a parametrization of measurement results [27], or through a combination of measurements and simulations, as is seen in [28].

A portion of the work in this thesis was spent on performing a light yield characterization of a liquid scintillator, similar to the work in [28]. Our method was based time of flight measurements of tagged neutrons from an AmBe source, together with MCNP PTRAC simulations to describe both energy depositions and time of flight. The method culminates in a fitted light yield function for that liquid scintillator. However, this work is not mature enough to be published yet.

J Adams measured two light yield functions for the NE213 and BC418 scintillators in the JET neutron camera, using scintillators similar to those installed in the camera [22]. These light yield functions are used in Papers I and II. The J Adams light yield function for NE213 scintillators describe the light yield L over two energy intervals as

$$L = \begin{cases} x_1 + y_1 \cdot E_p + z_1 \cdot E_p^2 + w_1 \cdot E_p^3 & : 0 < E_p \leq 1.85 \text{ MeV} \\ x_2 + y_2 \cdot E_p + z_2 \cdot E_p^2 + w_2 \cdot E_p^3 & : 1.85 < E_p \leq 16.74 \text{ MeV} \end{cases} \quad (2.4)$$

where E_p is the proton energy, and the remaining coefficients are found in Table 2. The J Adams light yield function for BC418 scintillators describe the light yield L over three energy intervals as

$$L = \begin{cases} x_3 + y_3 \cdot E_p + z_3 \cdot E_p^2 + w_3 \cdot E_p^3 & : 0 < E_p \leq 5.245 \text{ MeV} \\ x_4 + y_4 \cdot E_p + z_4 \cdot E_p^2 + w_4 \cdot E_p^3 & : 5.245 < E_p \leq 15.525 \text{ MeV} \\ x_5 + y_5 \cdot E_p + z_5 \cdot E_p^2 + w_5 \cdot E_p^3 & : 15.525 < E_p \leq 18.93 \text{ MeV} \end{cases} \quad (2.5)$$

where the remaining coefficients are found in Table 2. Both light yield functions are also displayed in Figure 12.

Table 2: Coefficients used in Equation 2.4 and 2.5.

i	x_i	y_i	z_i	w_i
1	0.0	0.1659	0.01049	0.01728
2	0.2012	0.2870	0.0378	-0.0011
3	0.0	0.0932	0.1014	-0.0068
4	-0.1393	0.2532	0.0472	-0.0014
5	-14.4633	3.8536	-0.2344	0.0057

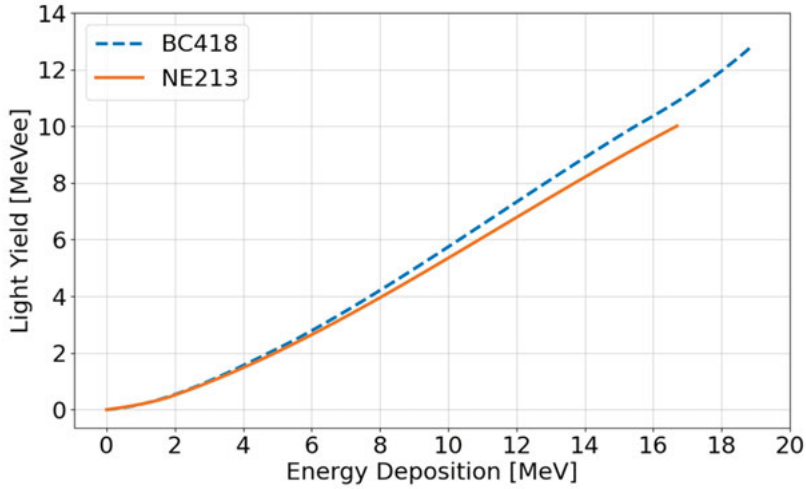


Figure 12: Light yield functions produced by J Adams for the NE213 and BC418 scintillators in the JET neutron camera.

The light yield function of a NE213 liquid scintillator has been of interest for a long time, and has therefore been measured by many other parties besides J Adams. A few of these measurements are listed here and compared with J Adams in Figure 13. J. Scherzinger measured the NE213 light yield response in 2016 using tagged neutrons in the 2-6 MeV energy range [29]. K. Gul measured the light yield function with a coincidence technique in 1988 [30]. E. Dekempeneer uses the term proton light output function for their measurement with a time-of-flight method in 1986 [31]. W.W. Lindstrom performed Monte Carlo simulations to simulate the NE213 light yield function in 1971 [32].

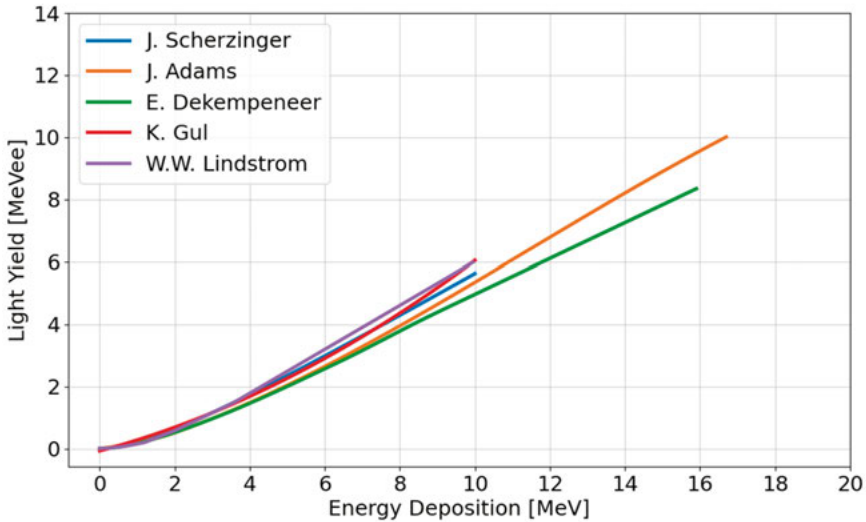


Figure 13: Estimated light yield functions for NE213 scintillators.

2.4 System Response Matrix

The detector response to incident particles can be simulated with a model of the detector. The type of response function obtained in this way can vary. In the context of neutron detection with scintillators, specifically for Papers I and II, the response is the simulated scintillator light yield spectrum. This necessitates an appropriate light yield function for the model, see section 2.3.5 Light Yield Functions. For Paper III, the response function instead describes the relative signal intensity in a scintillator array.

Since the naming conventions around response functions may vary, the definitions used in this thesis are presented below.

2.4.1 Definitions

A detector response function is based on a model of the detector, or just the scintillating material in a simplified model. The response is specified for one simulated neutron energy. A detector response matrix is created from a range of neutron energies. It can be folded with a neutron energy spectrum through a matrix multiplication, to yield a response that reflects the full spectrum.

A system response function is a model of the larger detector system, rather than just the detector. This may include materials such as collimators or detector shielding, and magnetic systems that impact charged particles.

2.4.2 Examples

In Papers I and II, the system response function for the JET neutron camera incorporates the effect of neutron scattering, proton scattering, and transmission through materials. The neutron camera detectors are housed in sealed detector boxes with a significant amount of magnetic shielding. This makes inclusion of in-scatter and transmission especially important here. The system response matrices from Papers I and II are found in Figure 14 and Figure 15 respectively.

In Paper III, the MPRu system response matrix is based on a model which simulates neutrons impinging on the converter foil. It then follows recoil protons through the magnetic system, to a scintillator on the hodoscope, see part 4. The MPRu. This system response matrix can be seen in Figure 16.

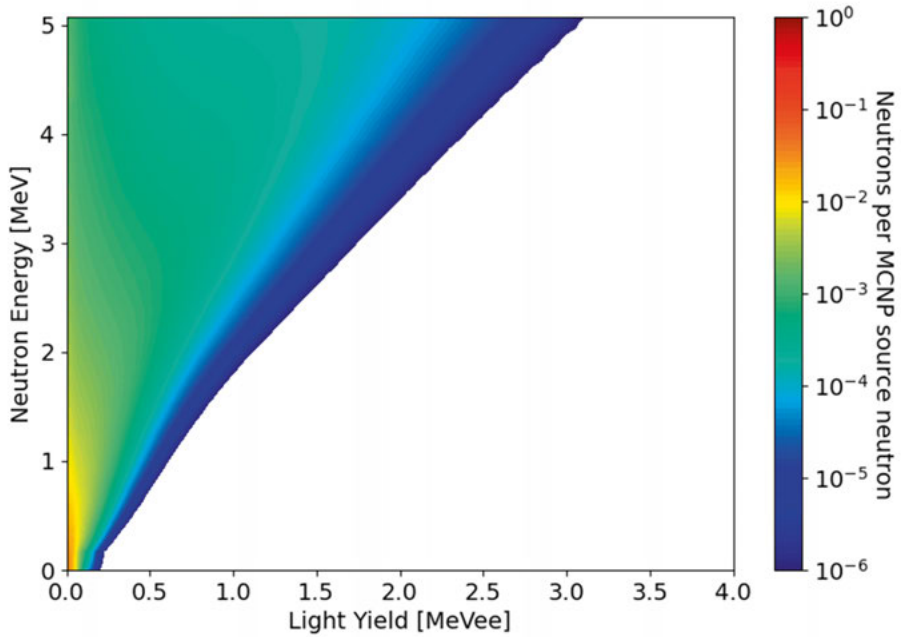


Figure 14: System response function for one channel of the JET neutron camera in Paper I, simulated for neutron energies around the average DD neutron energy of 2.45 MeV.

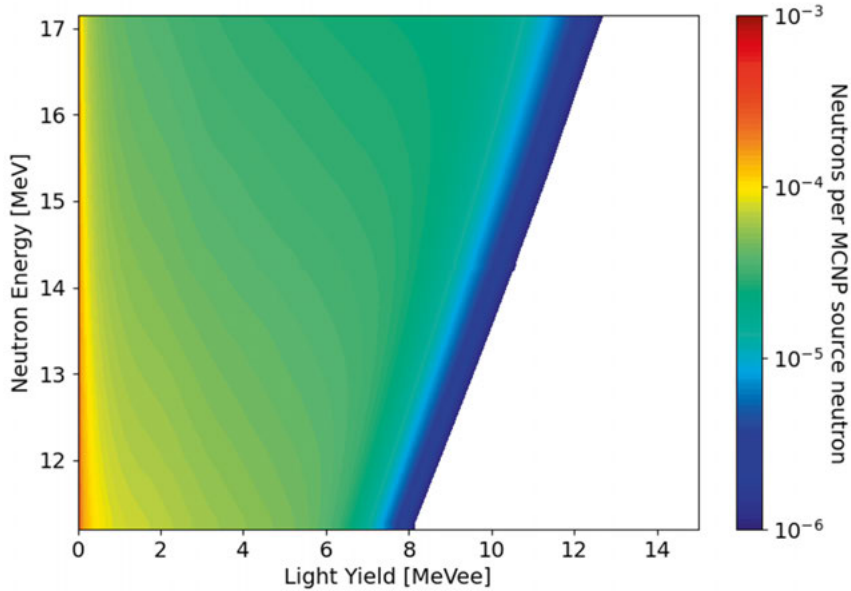


Figure 15: System response function for one channel of the JET neutron camera in Paper II, simulated for neutron energies around the average DT neutron energy of 14 MeV.

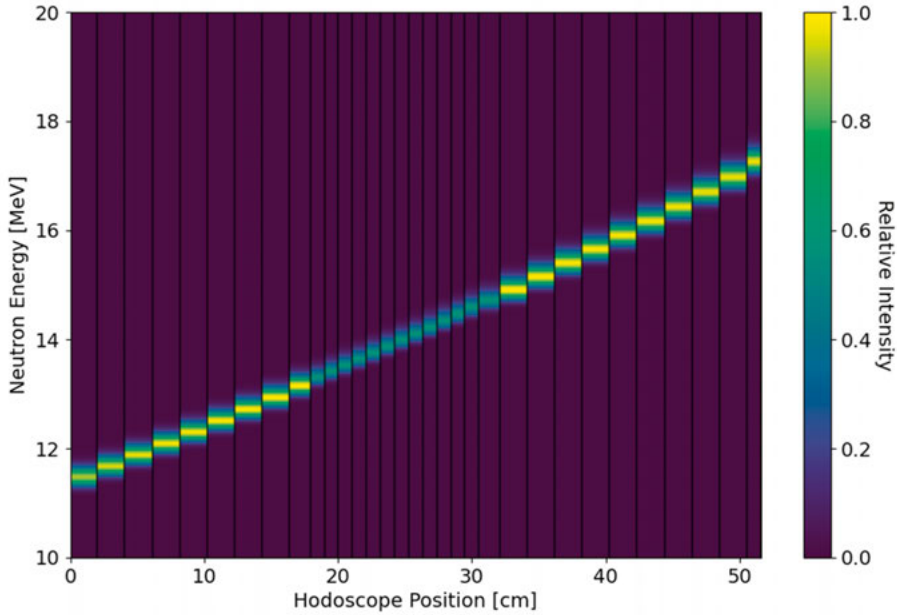


Figure 16: System response function for the MPRu in Paper III, describing the relative intensity in each hodoscope detector. The dark vertical lines mark the edges between detectors.

2.4.2 Light Yield Thresholds

A model is rarely able to describe the full light yield spectrum, and it is usually at its weakest for low light yields where background events are frequent. A lower light yield threshold applied on both the measured and simulated light yield spectrum can improve agreement between the two. Light yield thresholds are used in Papers I and II for this purpose.

2.5 Measurement Techniques

2.5.1 Proton Recoil Scintillators

This technique has been the main focus of part 2. Neutron Detection, and is the most straight-forward use of scintillator detectors. The detectors are placed in a neutron flux. Then neutrons interact with protons in the hydrogen-rich scintillator through elastic scattering, which then give rise to a scintillation light yield. The technique is used for the JET neutron camera in Papers I and II, with some exceptions from the exact methods laid out in this part. This is discussed in part 3. The JET Neutron Camera.

2.5.2 Thin-Foil Proton Recoil

Collimated neutrons impinge on a thin foil. The neutrons undergo elastic scattering on the protons of the foil. Recoil protons that escape the foil can then be detected with any kind of detector that is sensitive to charged particles. Forward-scattered protons will have an energy close to the incident neutron energy. Detectors utilizing this technique can obtain high-resolution neutron energy measurements.

The MPRu in Paper III uses proton recoil from a hydrogen-rich foil with a magnetic field to momentum-separate forward-scattered protons, see part 4. The MPRu.

The technique is also used in proton recoil telescopes, both with plastic (polyethylene) films [33] and silicon detectors [34].

2.5.3 Fission Chambers

A fission chamber is an ionization chamber lined with a fissile material, typically a Uranium isotope, which enables the ionization current. The chamber is filled with a gas, commonly Argon. When an energetic particle moves through the gas, it leaves a trail of ionized gas molecules in its wake. An electric field collects the electric charge from the ionization onto an electrode [10]. In the case of neutron detection, the neutrons fission the fissile material and the fission fragments ionizes the gas.

JET uses three pairs of fission chambers to monitor the neutron flux. These fission chambers together with activation foil measurements carry the JET neutron calibration [35] [36].

3. The JET Neutron Camera

The neutron camera is a well-established diagnostic system at JET. With its multi-sightline view of the plasma it is used to monitor a 2D profile of both the DD and DT neutron emission. The neutron camera has been involved in the measurements of fusion plasma quantities such as the ion temperature [37] [38], the ion densities [39], and the fraction of thermal neutron emission [40]. DT measurements from the camera have also been used to estimate the neutron yield in trace tritium experiments [41]. It was also used to estimate the neutron yield in a combined study with the MPRu [42]. Its data acquisition system has since been upgraded to a fully digital system, which allows for a more detailed data analysis than what was previously possible. A large part of the work in this thesis has been devoted to developing methods and data analysis procedures, to fully utilize and capitalize on this upgrade. This resulted in Papers I and II, in which methods for estimating the total neutron yield from DD and DT plasmas, using only neutron camera data and modeling, are presented.

The works in Papers I and II utilize the data acquisition, data reduction, and light yield calibration methods from sections 2.1 Data Acquisition, 2.2 Data Reduction, and 2.3 Light Yield Calibration respectively. Specific data reduction methods are detailed here in section 3.2 Data Reduction Specifics, while the resulting measurement data is shown in section 3.3 Measurement Data. The modelling used to connect measurement data to the underlying neutron emissivity profile of the plasma is detailed in section 3.4 Models and Simulations. The analysis culminates in DD and DT estimates of the volume integrated neutron yield, see section 3.5 Neutron Yield Estimates.

3.1 Instrument

The JET neutron camera has 19 lines of sight, each equipped with one NE213 and one BC418 scintillator. The detectors in each sightline are often referred to as detector channels, or simply channels. The neutron camera is divided into a horizontal part, containing channels 1-10, and a vertical part, for channels 11-19. The collimation of each channel is done with two rotatable steel collimators, which can be switched between two aperture settings. For DD operation, the collimator aperture typically is set to a diameter of 21 mm, for

DT operation, where higher fluxes are expected, it is instead set to 10 mm. An illustration of the neutron camera and its sightlines is found in Figure 17.

Each channel has a detector box containing two scintillators (NE213 and BC418), their PMTs, and a ^{22}Na gamma source for light yield calibration. The box also provides much-needed magnetic shielding for the PMTs. The detector box and its interior is illustrated in Figure 18.

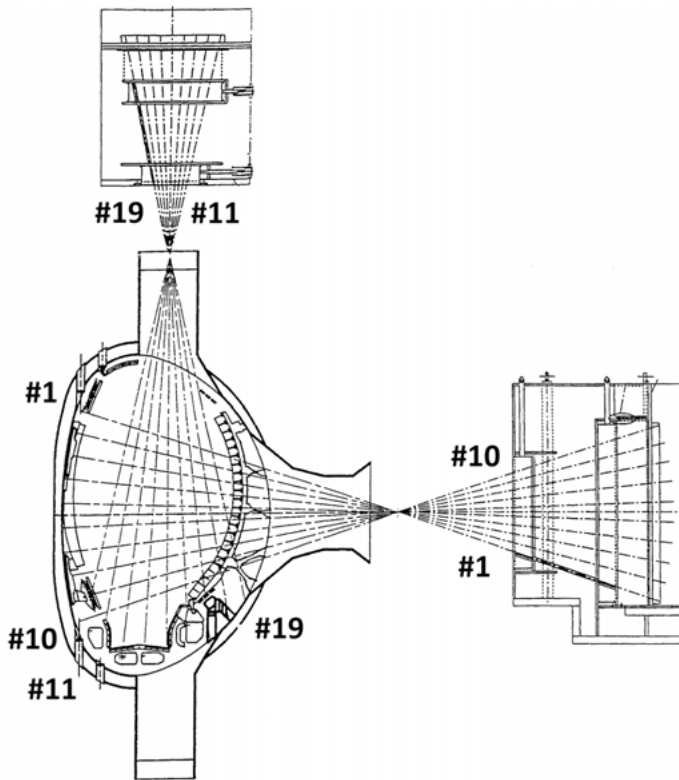


Figure 17: A poloidal cross-section of the horizontal and vertical JET neutron camera, with its 19 lines of sight through the JET torus. Adapted from JG96.200-3c in the JET Figure Database [43], Copyright by EFDA-JET.

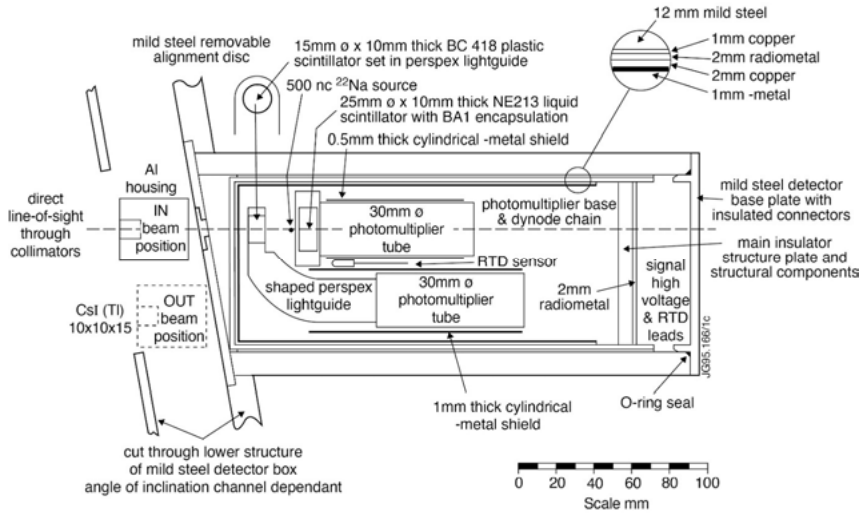


Figure 18: Illustration of a detector box in the JET neutron camera. Reference number JG95.166-1c in the JET Figure Database [43], Copyright by EFDA-JET.

3.2 Data Reduction Specifics

3.2.1 Dynamic Record Lengths

The neutron camera has collected large amounts of measurement data during the experimental campaigns at JET. Data records from a single large JET plasma discharge can add up to over 800 million samples in total with the current data acquisition system. This amount of data can be demanding for a data reduction code.

The works in Papers I and II use a Python data reduction code, primarily utilizing the NumPy and SciPy packages. Typically, equal-sized data records from the digitizer are stored as rows in a matrix, which allows for expedient vectorization. However, the dynamic record length setting (see section 2.2.4 Pile-Up), necessitates a different storage method. Data records are instead stitched together and stored as a single array of pulse shapes, here referred to as the pulse train, with complementary arrays denoting the start indices, record lengths, and time stamps for each record. This data structure is not compatible with vectorization for processing a large number of records. In order to enable vectorization, equal-sized records must first be extracted from the pulse train.

First, a pulse identification routine is used on the pulse train. The complementary start index array is disregarded in favour of the SciPy function `find_peaks`. This function returns the index number of prominent peaks, notably including pile-up events. Each pulse is also assigned a time stamp based on the record they originally belonged to, and how far along within that record the pulse appears.

A fixed width of samples around each pulse are then extracted as equal-sized records. This extraction of data records can be done by simply looping through the number of found pulses and slicing the pulse train array around each peak index. Although, a faster method to extract equal-sized records was developed for the works in Papers I and II. This method is based on the NumPy function `as_strided` [44], which manipulates the internal data structure of the NumPy array. In a preliminary study, the two methods were compared for a pulse train with 800 million samples, containing 25 million pulses. The stride method performed the extraction five times faster than the looping method. However, this time saving is far outweighed by the time required for `find_peaks` to identify the 25 million pulses in the pulse train. As a result, the stride method is not a significant upgrade for this application, until a faster alternative to `find_peaks` is found.

3.2.2 Pile-Up Treatment

Pulses that are too close together based on their assigned timestamps are marked as pile-up events. In Paper II, the limit is set at pulses within 100 ns of one another. These require special treatment in several ways.

During the baseline subtraction, the baseline is averaged from the pre-trigger samples. However, only the first pulse in a group of pile-up events has pre-trigger samples. The equivalent pre-trigger samples for subsequent pulses in the group do not represent the baseline, as seen in Figure 8. To address this, groups of pile-up events are identified in the data reduction code. All events in the group use the same average background as calculated for the leading pulse. This method functioned well, but did ultimately not have an impact on the data reduction in Paper II, as is evident from the next special treatment.

The pulse areas of pile-up events are very likely to be inflated by neighbouring pulses, which compromises their light yield values. Because pile-up and non-pile-up events originate from the same neutron energy distribution, they should also have a similar light yield spectrum. As a result, we can use the light yield spectrum of the non-pile up events, and scale it up based on the number of pile-up events. This method is used in Paper II where the high event rates of the DT experiments result in large fractions of pile-up events. It is possible that a pile-up reconstruction algorithm, as mentioned in section 2.2.4 Pile-Up, could perform better here. However, individual reconstruction treatment of millions of pile-up events, which is a typical amount for some of the largest JET plasma discharges, could be a time-consuming process.

3.3.3 Gamma Discrimination

Neutron measurements with the JET neutron camera require some form of gamma discrimination. In Paper I, the NE213 scintillators allow for the PSD analysis described in section 2.2.3 Pulse Shape Discrimination. However, the

BC418 scintillators in Paper II cannot distinguish between neutron- and gamma-induced events. Instead, gamma events are discriminated using a 6 MeVee lower light yield threshold, approximately corresponding to the full deposition of a 10 MeV neutron. For DT plasmas, events above that threshold are expected to be dominated by DT neutrons. This, in combination with the mechanical discrimination mentioned in section 2.1.1 Scintillators, provides a discrimination of most gamma events.

3.3 Measurement Data

The data reduction process produces a measured light yield spectrum for each detector channel, as exemplified in Figure 19. A light yield threshold of 0.5 MeVee is applied for the DD estimate, and 6 MeVee for the DT estimate. These same light yield thresholds are used in the models and simulation in each work. The sum of events above the light yield threshold from each channel are arranged in a neutron count profile, see Figure 20.

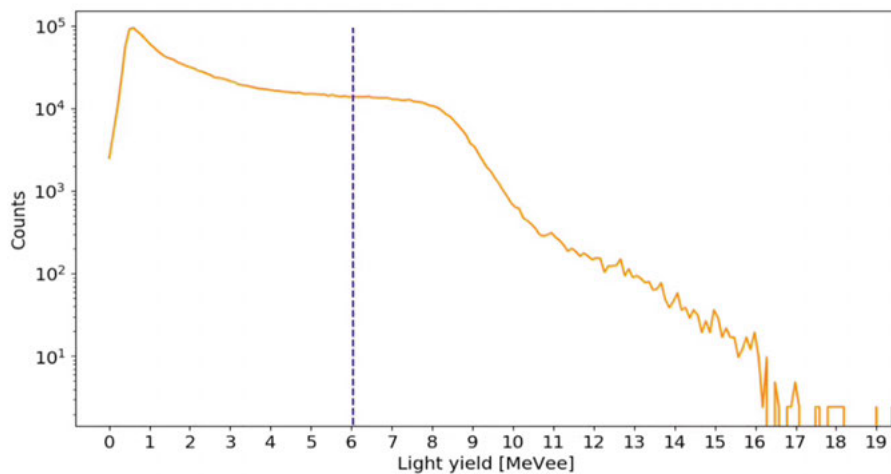


Figure 19: Light yield spectrum from Paper II, detector channel 15. The dashed blue line marks the light yield threshold at 6 MeVee.

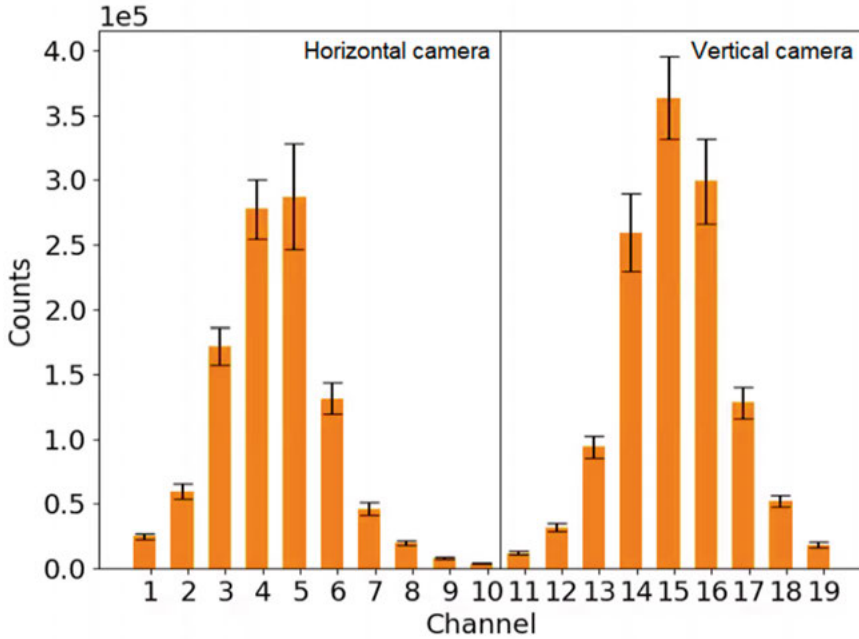


Figure 20: Neutron count profile from Paper II. The error bars are bases on the uncertainty of the light yield calibration.

3.4 Models and Simulations

This section describes the set of models used to connect the measured neutron count profile to the underlying neutron emissivity profile in the plasma. We adapt a “forward modeling” approach, i.e., the aim is to calculate the simulated neutron count profile expected from a given neutron emissivity profile. The shape and intensity of the neutron emissivity profile is determined by a set of free parameters. These parameters can be varied in a fit until a good agreement between the measured and simulated neutron count profiles is found. This results in an estimate of the neutron emissivity profile, supported by the neutron camera measurement data. The neutron yield is then obtained by integrating the fitted neutron emissivity profile over the entire plasma volume.

The modeling considers three different categories of neutrons that reach the detector; direct, in-scatter, and backscatter neutrons. Direct neutrons reach the detectors without scattering in any material on its way from the fusion plasma. In-scatter neutrons first scatter against in some material near the detector, and backscatter neutrons first scatter against the torus back wall [45]. The neutron energies for each category are covered in section 3.4.2 Neutron Energies.

The direct neutrons are simulated with the optical model LINE2.1, see section 3.4.3 LINE2.1, which calculates the direct neutron rate on each detector for a given neutron emissivity profile model, see section 3.4.1 Neutron

Emissivity Profiles. The simulated direct neutron rates are combined with the system response matrix in section 3.4.4 System Response. Finally, the simulated neutron count profile is compared to the measured neutron count profile in section 3.4.6 Neutron Emissivity Profile Fit.

3.4.1 Neutron Emissivity Profiles

Papers I and II use different models to describe the neutron emissivity Δ from a poloidal slice of the plasma. In Paper I, the model assumes that the neutron emissivity is constant on the magnetic flux surfaces of the plasma, as

$$\Delta = r_n(1 - \rho^2)^\alpha, \quad (3.1)$$

where r_n is a scale factor, ρ is the normalized minor radius, and α is a peaking parameter. The central position of these flux surfaces and the normalized minor radius ρ are both determined by EFIT++/JEC2020 [46]. This simplified model does not fully reflect the complexity of a fusion plasma, for instance, neutron emission from trapped particles is not well described by the model [47]. It is also fairly static as only α is used as a fitting parameter. An example of this neutron emissivity profile is found in Figure 21.

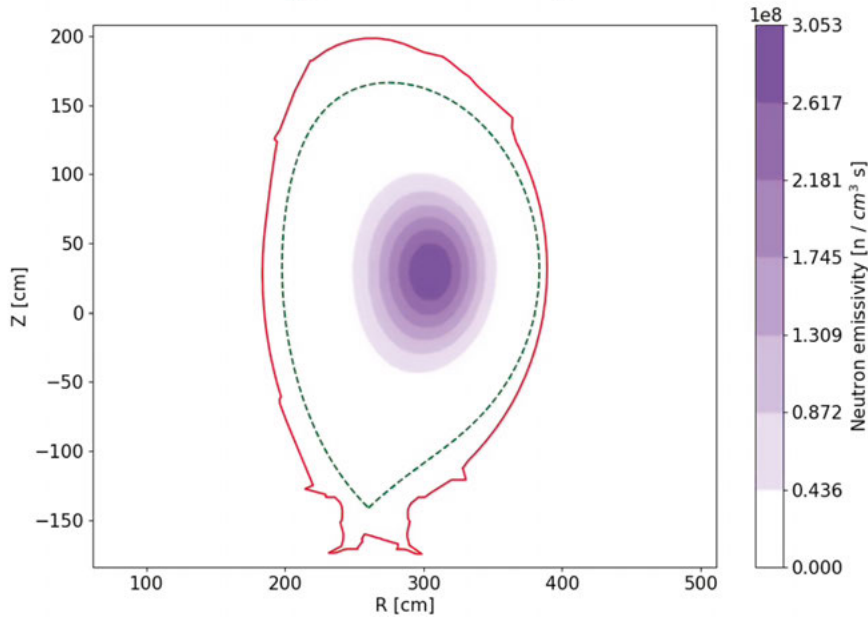


Figure 21: Neutron emissivity profile model from Paper I. The dashed green line is the separatrix, which marks the last closed magnetic flux surface, the solid red line marks the first wall of the tokamak.

In Paper II, the neutron emissivity is described by a 2D Gaussian as

$$\Delta = r_n \cdot e^{-\left(\frac{(R-R_0)^2}{2\sigma_R^2} + \frac{(Z-Z_0)^2}{2\sigma_Z^2}\right)} \quad (3.2)$$

where R is the major radius, (R_0, Z_0) denote the central position of the Gaussian, and σ_R & σ_Z are the standard deviations in the R- and Z-directions respectively. This model does not rely on the assumptions made for Equation 3.1, and it is much more flexible as R_0 , Z_0 , σ_R , and σ_Z are all fitting parameters. An example of this neutron emissivity profile is found in Figure 22.

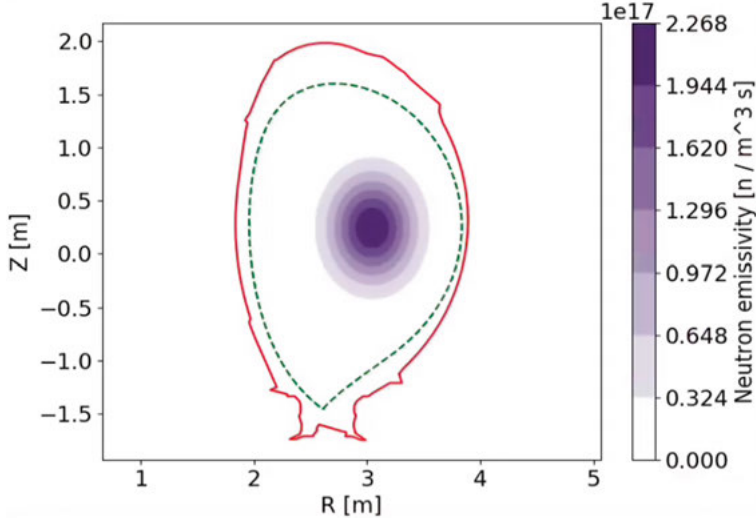


Figure 22: Neutron emissivity profile model from Paper I. The dashed green line is the separatrix, which marks the last closed magnetic flux surface. The solid red line marks the first wall of the tokamak.

While both of the models used in Papers I and II are simplifications, they seem to be sufficient for the purpose of estimating the volume integrated neutron yield. In a preliminary study reported in Paper II, the 2D Gaussian model was compared to a more advanced model by the plasma transport code TRANSP [48]. The DT neutron yield estimate was performed with both the 2D Gaussian and the TRANSP model, and the resulting neutron yields were within 6% of one another. This suggests that the 2D Gaussian model is not overly simplified for our purposes.

3.4.2 Neutron Energies

The direct neutrons from the neutron emissivity model are set to be monoenergetic, 2.5 MeV for DD neutrons and 14 MeV for DT neutrons. This simplification was implemented to have the method be reliant on as few codes and measurement diagnostics as possible. In future works, the neutron energy spectrum from the plasma could be simulated using transport codes such as TRANSP or ASCOT [49], together with the DRESS code [50].

The backscatter neutrons are modeled with dedicated MCNP models for DD or DT plasmas. The neutron sources used in these models are representative of the gross features of a typical JET high performance plasma [22]. The

simulated neutron energy spectra at the BC418 and NE213 scintillators in channel 15 are shown in Figure 23 and Figure 24 respectively.

For the DT estimate, most of the backscatter neutrons are well below the light yield threshold of 6 MeVee (approximately corresponding to a neutron energy of 10 MeV). The DD estimate, however, uses a light yield threshold of 0.5 MeVee (approximately corresponding to a neutron energy of 2 MeV). This makes the backscatter component of the neutron emission much more impactful for the DD estimate. According to a study in [45], these backscatter energy spectra are very insensitive to changes in the shape of the neutron emissivity profile.

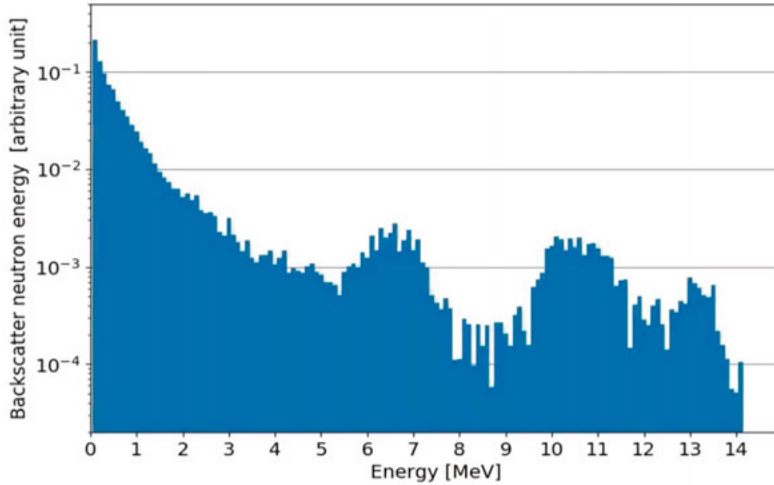


Figure 23: Neutron energy spectrum for backscatter neutrons at the BC418 detector in channel 15, simulated in MCNP for a DT plasma.

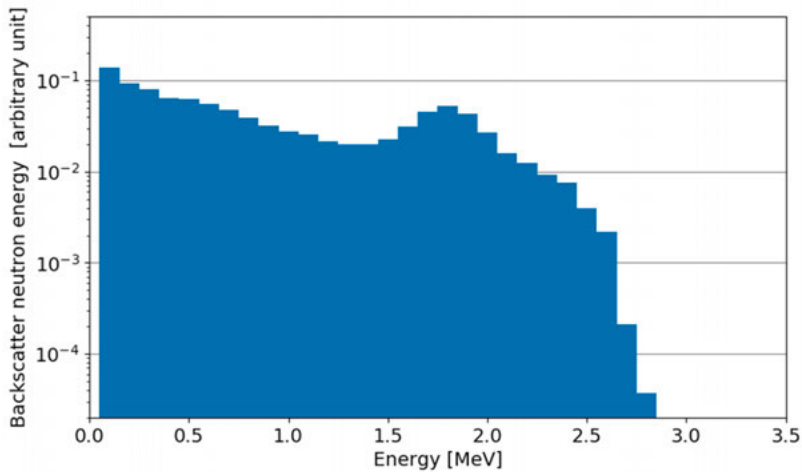


Figure 24: Neutron energy spectrum for backscatter neutrons at the NE213 detector in channel 15, simulated in MCNP for a DD plasma.

3.4.3 LINE2.1

In the LINE2.1 model of the JET neutron camera, all materials are treated as perfect absorbers. It divides the tokamak volume into voxels, then simulates isotropic emission from random positions within each voxel. The code draws lines from the emission point to a random point on the detector, and checks if it passes through the collimator without collision, see Figure 25. Each voxel is assigned a visibility score, depending on how likely emissions from that voxel are to reach a certain detector.

For a specific detector channel, the model only considers the voxels in the LOS of that channel. The resulting visibility cones from LINE2.1 are shown in Figure 26. The neutron emission from each voxel is calculated with the voxel volume and the neutron emissivity profile model. The direct neutron rate is simulated by scaling the neutron emissivity with the visibility score, and summing the resulting value from each voxel in the LOS.

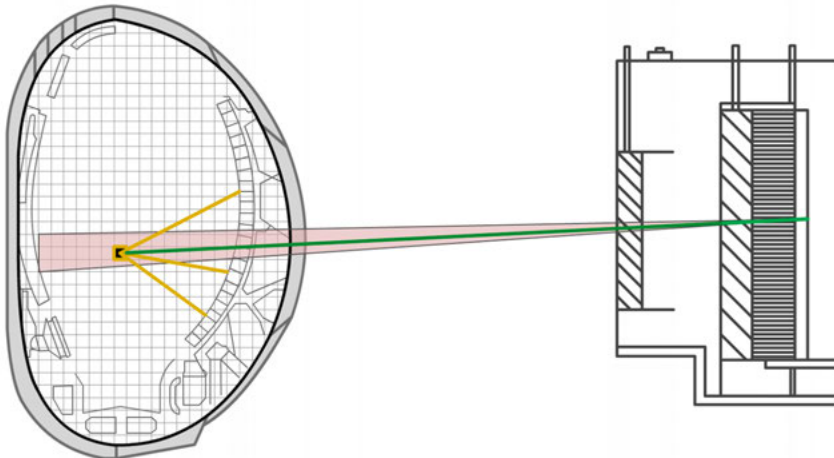


Figure 25: An illustration of the LINE2.1 concept in a poloidal slice of the torus. Four emissions are emitted from a voxel in the detector LOS. The emission line marked in green reaches the detector without any collisions.

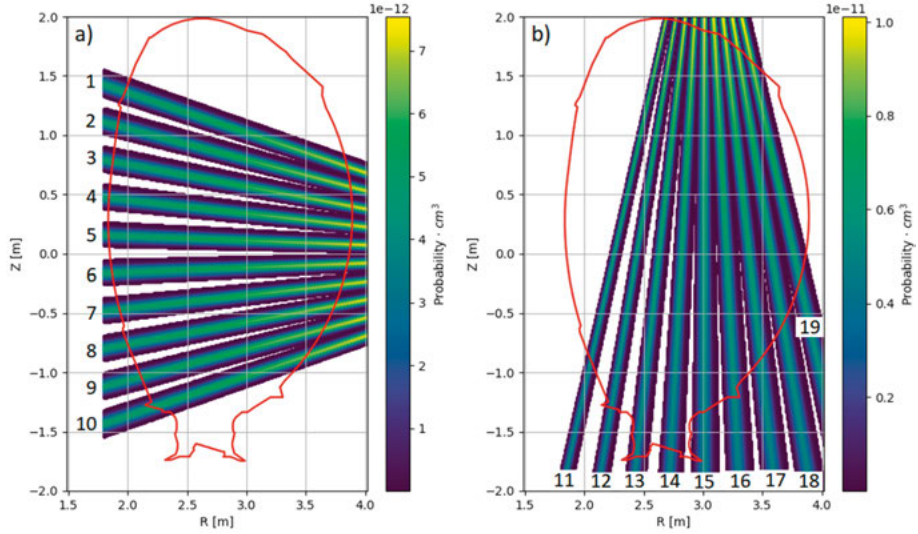


Figure 26: LINE2.1 visibility cones, shown for the horizontal camera in (a) and the vertical camera in (b). The probability shows the visibility scores across the poloidal slice. The solid red line marks the first wall of the tokamak.

3.4.4 System Response

The aim of this section is to relate the direct neutrons from section 3.4.3 LINE2.1, to a simulated light yield spectrum, while also accounting for in-scatter and transmission through obstructing material.

The system response matrices used in Papers I and II are constructed using two MCNP simulations of the JET neutron camera. The first simulation imitates the optical LINE2.1 model by treating all materials as perfect absorbers. It calculates the total number of neutrons N that reach the detector.

The second simulation enables neutron scattering and transmission, and calculates the simulated light yield spectrum S_L . This is done using a combination of the f6 and f8 MCNP tallies. The f6 tally estimates the light yield from proton energy depositions, using the dose energy and dose function cards to implement the J Adams light yield function. The f8 tallies the energy distribution of pulses, and the PHL option directs it to tally the light pulses from the f6 tally.

Both the first and the second simulation use the same monoenergetic neutron source at the entrance of the first neutron collimator. As a result, the scaled simulated light yield spectrum S_L/N describes the increase in neutron rate due to in-scatter and transmission, compared to the optical case that the first simulation emulates. The two simulations are performed for a range of neutron energies to create a system response matrix. The completed system response matrices are found in section 2.4.2 Examples.

Due to the monoenergetic simplification detailed in section 3.4.2 Neutron Energies, the system response matrix is not folded with a neutron energy spectrum as in Equation 2.6. Instead, the S_L is obtained from the matrix row corresponding to the direct neutron energy, just as for a system response function. A Gaussian broadening from the light yield calibration, see section 2.3.3 Gamma Calibration, is also applied to S_L for each detector channel.

The sum of the simulated light yield spectrum S_L above the light yield threshold produces an efficiency factor f_i for channel i . This efficiency factor is applied to the simulated direct neutron rate, to account for in-scatter and transmission. In Paper I, the impact of including in-scatter and transmission in the simulation was estimated. The in-scatter and transmission inclusions contributed 5.6% and 3.4% respectively to the simulated neutron rate above the light yield threshold.

3.4.5 Backscatter

Backscatter is simulated in a separate MCNP model for both Papers I and II, which produces a backscatter neutron spectrum. This spectrum is in the units of neutrons per the number of units produced in the plasma. In our method, the backscatter model does not interface with the neutron emissivity profile model directly. Instead, the backscatter neutron spectrum is scaled with the volume integrated neutron yield from that neutron emissivity profile. The scaled spectrum is then folded with the system response matrix to produce a backscatter light yield spectrum. The backscatter neutron rate is obtained by summing events in the spectrum above the light yield threshold.

3.4.6 Neutron Emissivity Profile Fit

The simulated neutron rate, obtained from the simulated light yield spectrum in section 3.4.4 System Response, in each channel is converted to neutron counts for the time interval of a specific measurement. These values are then arranged in a simulated neutron count profile. This profile is compared to the measured neutron count profile.

The scale factor r_n from Equations 3.1 and 3.2 is set such that the sum of the measured neutron count profile is equal to the sum of the simulated neutron count profile. In Paper I, the shape difference between the two count profiles is described by the CSTAT test statistic. The fit is performed by varying the fitting parameters of the neutron emissivity profile to minimize CSTAT. In Paper II, the shape difference is instead described by the Poisson log likelihood, and the respective fitting parameters are varied to maximize the Poisson log likelihood in a Markov Chain Monte Carlo algorithm [51]. The specific steps for the fits are laid out in Papers I and II. An example of a completed fit from Paper II is shown in Figure 27.

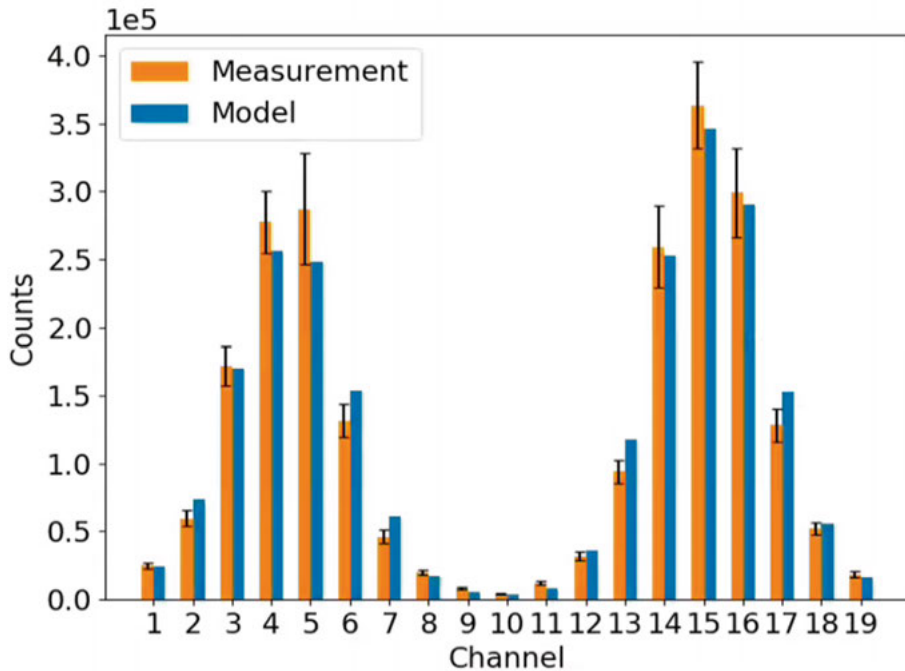


Figure 27: Measured and simulated neutron count profiles from Paper II, after a completed neutron emissivity profile fit. The uncertainties on the measurement data is propagated from uncertainties in the light yield calibration.

3.5 Neutron Yield Estimates

The volume integrated neutron yield Y_N is estimated based on a fitted neutron emissivity profile, which is evaluated on a poloidal grid. The emissivity values are integrated toroidally, then summed over all grid values to calculate Y_N .

The Y_n estimates from the JET neutron camera are compared with corresponding estimates by the JET fission chambers [35] [36], see section 2.5.3 Fission Chambers. In Paper I, the DD neutron yield is estimated with results shown in Figure 28, where the fission chambers estimate a 9.6% higher DD neutron yield on average.

In Paper II, the DT neutron yield is estimated, with the results shown in both Figure 29 and Figure 30. These estimates were calculated for the two JET experimental campaigns DTE2 [52] and DTE3 [53]. The comparison in this work shows instead that the neutron camera estimates a higher DT neutron yield on average, 32% higher for DTE2 and 42% higher for DTE3.

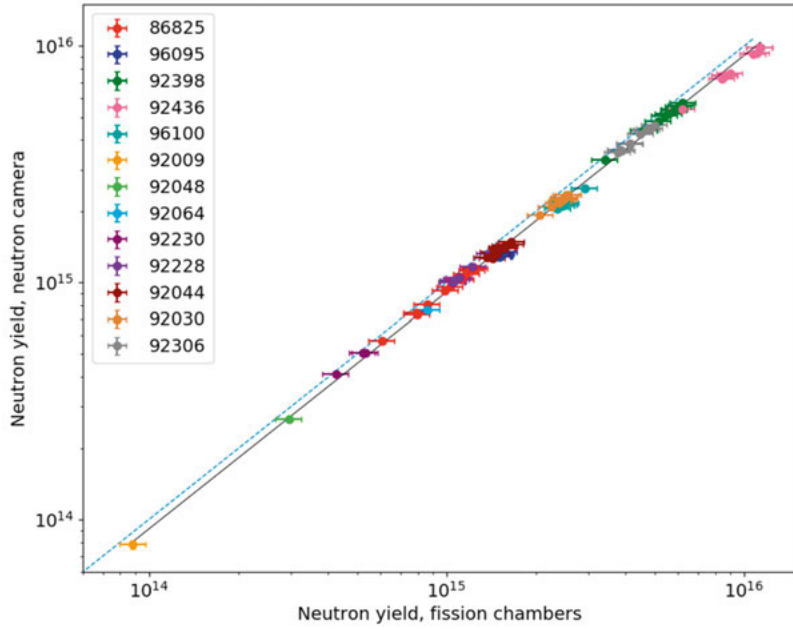


Figure 28: Neutron yield estimates with the neutron camera from Paper I, versus the estimate by the fission chambers. Calculated for several time intervals from 13 different JET plasma discharges. The black dashed line has a slope of 1, corresponding to a perfect agreement between the two.

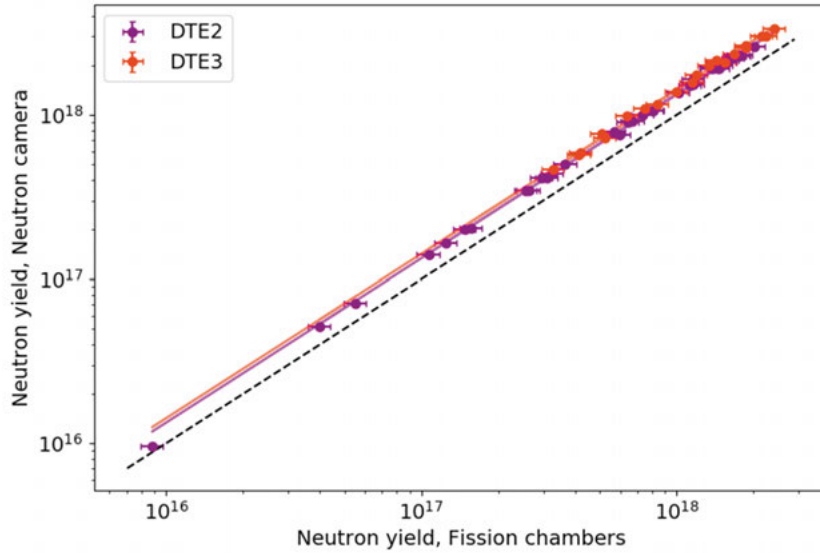


Figure 29: Neutron yield estimates with the neutron camera from Paper II, versus the estimate by the fission chambers. Calculated for 39 JET plasma discharges from the DTE2 campaign, and 20 from the DTE3 campaign. The solid purple and orange lines are fitted to the DTE2 and DTE3 datasets using orthogonal distance regression. Their slopes are 1.34 for DTE2 and 1.42 for DTE3. The black dashed line has a slope of 1, corresponding to a perfect agreement between the two.

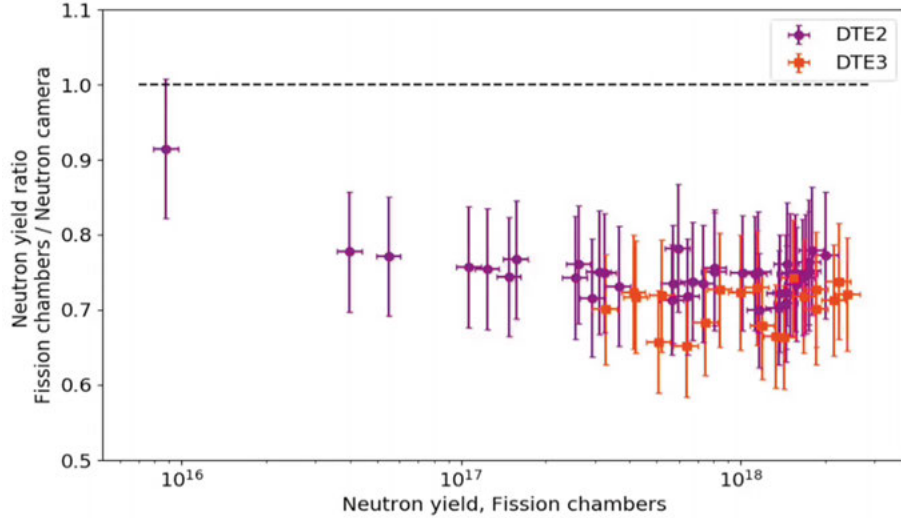


Figure 30: The ratio of neutron yield estimates between the fission chambers and the neutron camera, versus the fission chamber estimate. Based on the data in Figure 29.

3.6 Reflections on Papers I and II

3.6.1 Inconsistencies

From the comparisons in Figure 29 and Figure 30, it is clear that the DD and DT neutron yield estimates are inconsistent with the estimates from the fission chambers. They are also inconsistent with one another, since one is overestimating and the other underestimating the neutron yield compared to the fission chamber estimate. The reason for this inconsistency is not known. Conceptually, the estimates in Paper I and II use very similar methods. However, as is evident from this thesis, there are many areas where the DD and DT estimates use different techniques. Some differences, such as in the neutron emission profile models, could be eliminated to search for the origin of this inconsistency. The DD estimate could even adopt the thermal light yield calibration to that end. Other techniques, however, such as the pulse shape discrimination, have irreconcilable differences due to the two scintillator types.

3.6.2 Challenges

The DT estimate also comes with additional challenges, such the high rate of pile-up affecting the quality of data records. High count rates also cause a downshift of the measured light yield spectrum, an effect that is not replicated in the simulated light yield spectrum. Any discrepancies in the light yield calibration will greatly affect the neutron yield estimate.

One underlying systematic uncertainty for both estimates is the lack of up to date drawings of the JET neutron camera. Any major discrepancies in the models could have large ramifications for the estimates.

In future works, a closer comparison between the methods in Paper I and II should be made. There are ways to reduce differences between the methods to better understand, or perhaps eliminate, this inconsistency.

4. The MPRu

The upgraded Magnetic Proton Recoil (MPRu) high-resolution neutron spectrometer has been in operation at JET since 1996, and has seen several upgrades since then [15]. A high-resolution neutron diagnostic can be used to measure fusion plasma quantities such as alpha knock-on [54] [55], plasma heating [56] [57], and plasma rotation [58].

Paper III is the first exploitation of the measurement results of the MPRu from the DTE3 [53] experimental campaign. The work in Paper III uses MPRu measurements to investigate the plasma rotation and the thermonuclear emission, see sections 4.5 Results and 4.6 Reflections on Paper III. The work utilizes the data acquisition and data reduction techniques from sections 2.1 Data Acquisition and 2.2 Data Reduction, but in the context of a thin-foil proton recoil system, see section 4.1 Instrument. The PSD analysis is explained in section 4.2 Measurement Data, while additional data reduction techniques involving the PSD are explored in section 4.3 Data Reduction Exploration. The method in Paper III relies on models of the neutron spectrum and a system response matrix, which is covered in section 4.4 Modelling and Analysis.

4.1 Instrument

The MPRu is a thin-foil magnetic proton recoil spectrometer. It has a semi-tangential LOS which passes through the plasma centre twice. An illustration of a vertical cut through the MPRu is seen in Figure 1 from [15].

In the MPRu, collimated neutrons interact with protons in a hydrogen-rich foil through elastic scattering. The energy E_p of a recoil proton can be related to the energy E_n of the incident neutron as

$$E_p = E_n \cos^2 \theta_{np}, \quad (4.1)$$

where θ_{np} is the scattering angle in the laboratory system [15]. The energy of a forward-scattered proton is, to a good approximation, equal to the incident neutron energy. Forward-scattered protons are selected with a proton collimator, after which they enter the magnetic system. The protons are momentum-separated by the magnetic field and focused onto the hodoscope, a phosphor scintillator array.

The MPRu hodoscope has 32 phoswich scintillators, referred to as hodoscope channels. The scintillators have two different widths. Channels 1-9 and 23-32 are 20 mm wide, while the band of channels 10-22 are 10 mm wide.

The phoswich scintillators in the hodoscope have two scintillating layers. A thin layer with a light pulse decay time of 1.8 ns, and a thicker layer with a light pulse decay time of 180 ns. Neutrons with energies below around 5 MeV will stop in the thin layer, and protons above 18 MeV will escape the thick layer. As a result, protons with energies within that energy band will penetrate thin layer and be stopped in the thick layer, which yields a characteristic light pulse shape. Because the design is also sensitive to which direction a particle enters the phoswich scintillator from, random background events are likely to induce light yield pulses that can be distinguished from the measurement data.

The MPRu hodoscope is also equipped with an LED, which is used in system diagnostics. The full design is further detailed in [15].

4.2 Measurement Data

The PSD analysis applies a short and a long gate, shown in Figure 31. Light pulses from the thin phoswich layer will primarily give a signal in the short gate, but light pulses from the thick layer will give a signal in both gates due to its longer light pulse decay time.

The integrated pulse areas Q_{short} and Q_{long} for each respective gate are displayed in a 2D histogram. This is exemplified in Figure 32, which marks the proton peak and other features of the histogram.

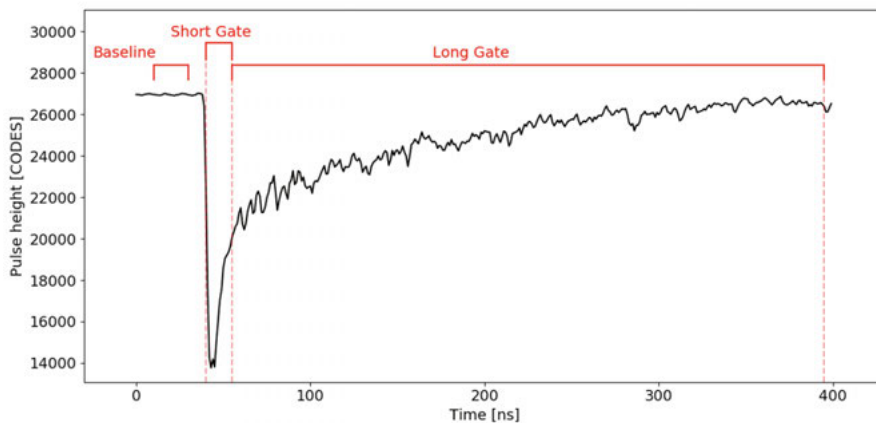


Figure 31: MPRu data record. Marked in red is the sample region used to average the baseline, and the short and long PSD gates.

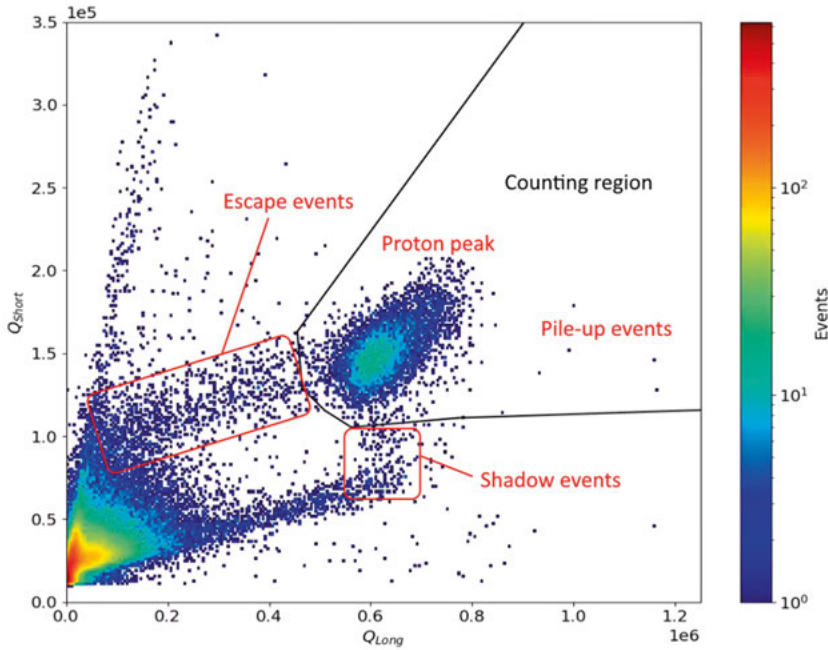


Figure 32: 2D histogram from the PSD analysis. The counting region determines which events are counted as proton events. Marked in red are specific features of the histogram.

Escape events and shadow events result from protons depositing energy in two adjacent scintillators in the array. From the perspective of one specific scintillator, an escape event leaves the scintillator too early and deposits less energy in the thick layer, leading to a smaller Q_{long} . A shadow event arrives from an adjacent scintillator and deposits less energy in the thin layer, leading to a smaller Q_{short} . This is illustrated in Figure 33. To avoid double counting, only one of these should count towards proton events across the hodoscope. The inclusion of escape events is explored in section 4.3.2 Escape Event Correction.

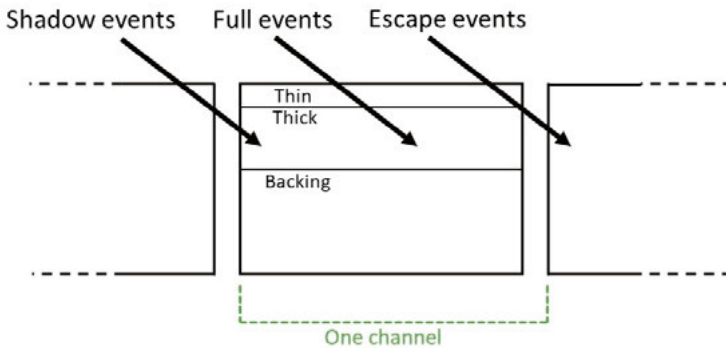


Figure 33: Escape, shadow, and full events entering a phoswich scintillator. The dashed green line indicates that full events and escape events belong to this channel.

The total number of proton events in a hodoscope channel is calculated by summing all events in the counting region shown in Figure 32. For the work in Paper III, the counting region was manually selected, though methods for a more systematic selection is explored in section 4.3.2 Escape Event Correction. Sums from all hodoscope channels are collected in a hodoscope histogram. Data from the same JET plasma discharge is shown in Figure 34 as proton counts in each channel, and in Figure 35 as proton counts/cm at the scintillator positions on the hodoscope. Note that channels 1 and 25 are inactive and do not produce any data.

The hodoscope histogram can be related to the incident neutron energy spectrum through a system response matrix, see section 4.4 Modelling and Analysis, where the peak around channel 13 and 14 corresponds to the 14 MeV neutron peak. As can be seen in Figure 34, there is also a large low-energy component in the hodoscope histogram, which is discussed further in Paper III. Though as a result of this component, channels 9 and below are excluded from the analysis.

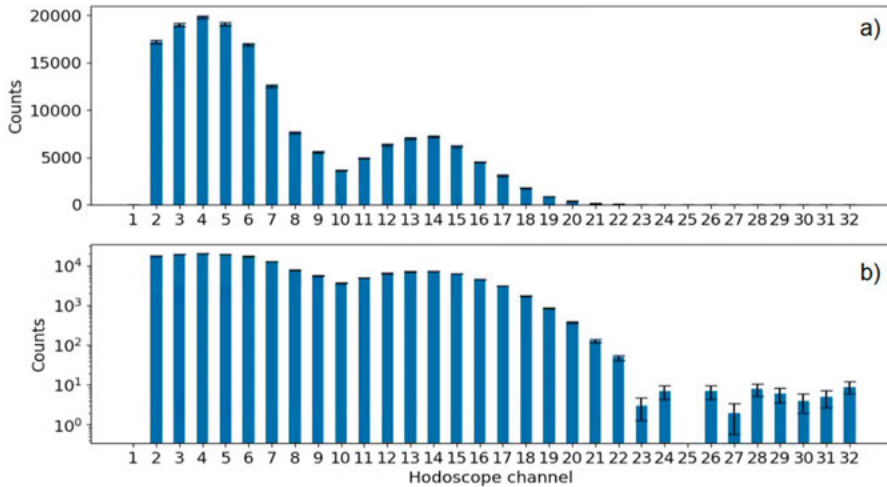


Figure 34: Summed proton counts in each hodoscope channel in linear (a) and log (b) scale.

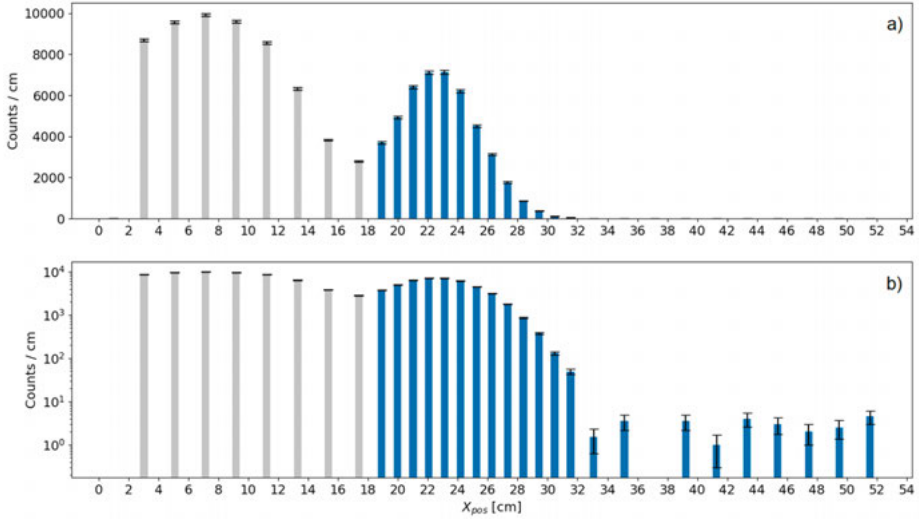


Figure 35: Summed proton counts per cm across the hodoscope in linear (a) and log (b) scale. Channels excluded from the analysis are marked in grey.

4.3 Data Reduction Exploration

The PSD aspect of the MPRu data reduction routine has many opportunities for improvement. This section explores a few techniques that were either not relevant for the discharges studied in Paper III, referring to section 4.3.1 LED Removal, or the technique was not mature enough to implement in the routine, as was the case for section 4.3.2 Escape Event Correction. Regardless, the development of these techniques made up a notable part of the analysis work.

4.3.1 LED Removal

The LED at the hodoscope gives a signal in each scintillator. Normally, the LED is switched on just before and after a neutron measurement, but is left off during the measurement. Unfortunately, this feature sometimes fails, leaving the LED on for the entire duration. In some instances, the group of LED events in the PSD 2D histogram can end up quite close to the proton peak, see Figure 37 a). For this reason, the mid gate was introduced in the PSD method. LED events have a distinctly different shape, see Figure 36, compared to proton events, see Figure 31, which the mid gate specifically captures.

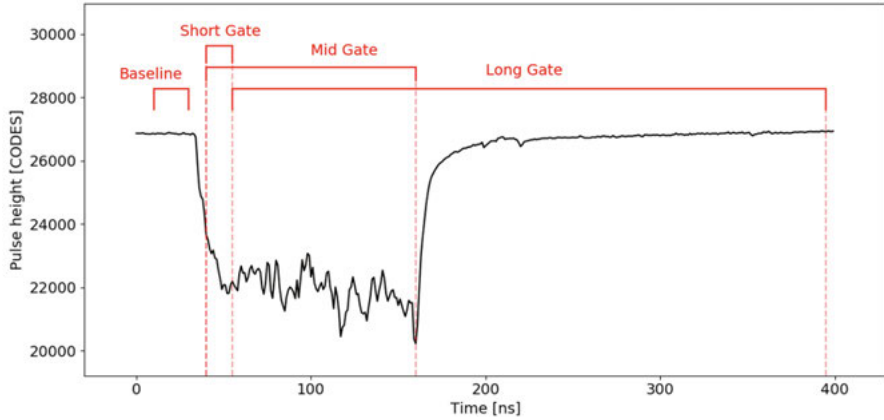


Figure 36: MPRu data record of an LED event. Marked in red is the sample region used to average the baseline, and the short, mid, and long PSD gates.

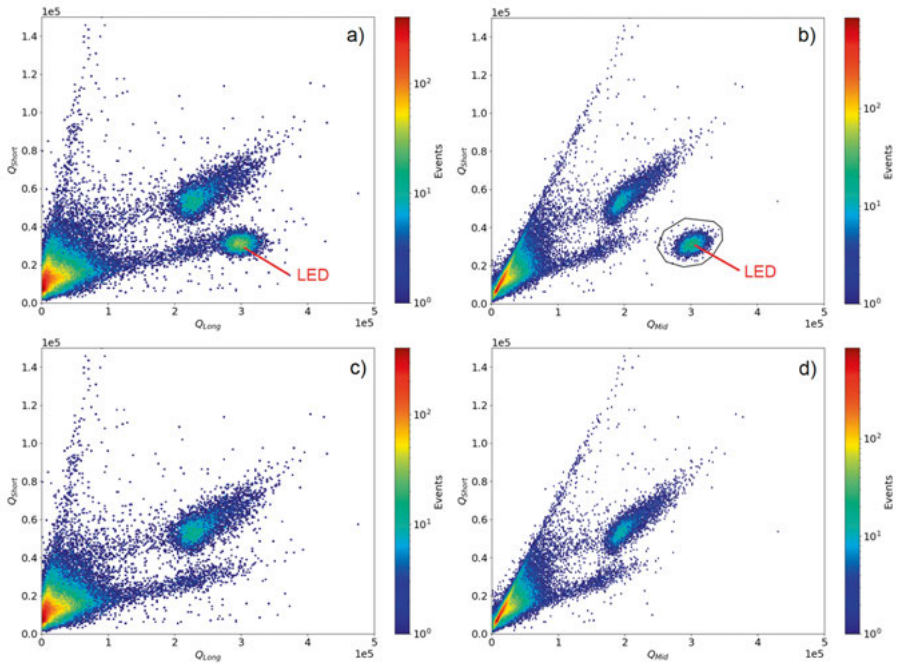


Figure 37: 2D histogram from the PSD analysis, using either the traditional short and long gate in (a) and (c), or the short and mid gate in (b) and (d). The LED events are removed using the PSD selection in (b). The top and bottom row shows the histograms before and after the removal.

The PSD analysis can use the short and mid gate to further separate LED events from the proton peak in the 2D histogram, see Figure 37 b). The LED events are identified through a PSD selection, which allows us to exclude them

in other configurations. The aftermath without the LED events is shown in Figure 37 c) and Figure 37 d) for different gates.

For the JET discharges studied in Paper III, this issue, when it appeared, was not obstructive enough to warrant LED removal.

4.3.2 Escape Event Correction

The total number of proton events should include the escape events defined in section 4.2 Measurement Data. Because these events blend in with the background events, they cannot be fully extracted with a PSD selection. They also cannot be easily separated from the background with a new gate, as is done in section 4.3.1 LED Removal, since the escape events by their nature have a range of possible pulse shapes.

Instead, Monte Carlo simulations can be used to estimate the fraction of escape events to the total number of proton events. This is done in an internal study for the scintillators in the hodoscope [59]. Some of the results from that study are shown as a cumulative fraction in Figure 38 a), and as a fraction in Figure 38 b).

The relative position, used in Figure 38, refers to the position of events along a straight line in the 2D histogram, where 1 is the centre of the proton peak. The earlier an escape event leaves the scintillator, the less energy it deposits in the thick scintillator layer. This results in a smaller Q_{long} value and a smaller relative position value. This continues until the relative position 0, beyond which would-be escape events instead miss the scintillator.

The cumulative fraction in Figure 38 a) shows the fraction of escape events that are not counted if the PSD selection would cut at a particular relative position. For example, a snug PSD selection around the proton peak might cut at the relative position 0.9, which would mean that approximately 11% of the total proton counts are left outside the PSD selection.

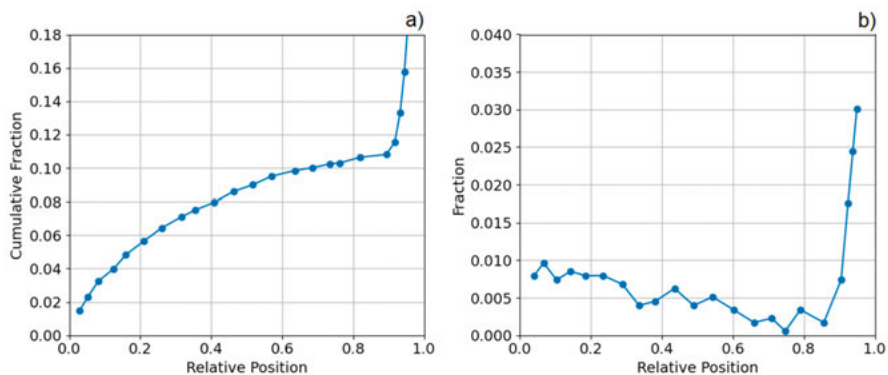


Figure 38: Monte Carlo simulation of the fraction (b) and cumulative fraction (a) of escape events in the MPRu hodoscope, at positions relative to the proton peak.

The relative position line is shown in Figure 39 a) for an example 2D histogram. In Figure 39 b), it is instead shown as a set of guidelines at 10% increments of the relative position. The solid PSD selection line in the same figure shows an example of where a snug PSD selection would cut across the escape events. The PSD selection line cuts at a relative position of approximately 0.75, which according to the cumulative fraction leaves around 10% of total proton events outside the PSD selection. The corresponding correction factor would then be 1.1, which would be applied to the sum of events in the counting region from Figure 32.

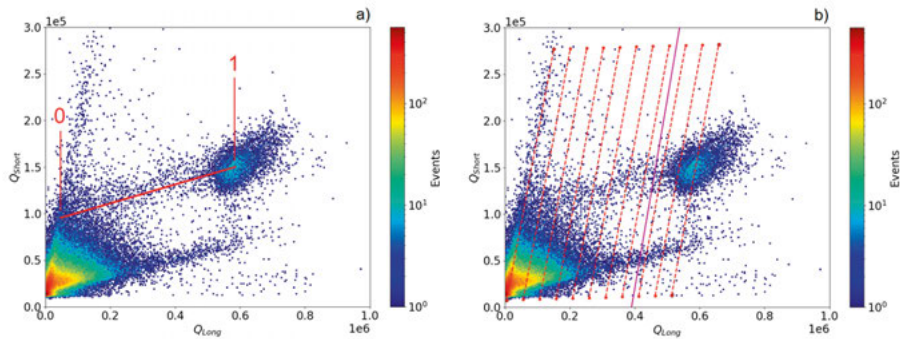


Figure 39: 2D histograms showcasing the relative position markers for escape event correction. The start and end points of the relative position is shown in (a). Percentile marker lines are shown in (b) together with a solid purple PSD selection line.

The PSD selection should strive to include as many of the measured escape events as possible, but it is not clear how far down in relative position one should go. A wide PSD selection may instead include too many background events, which compromises the result. This selection could be aided by a comparison between the simulated fraction in Figure 38 b), and a similar fraction calculated from measurement data.

The 2D histogram in Figure 40 has ten counting regions to measure the amount of escape events. The sum of events in each region estimate the number of escape events. By dividing the number of escape events with the total number of events in the proton peak (as done with the counting region in Figure 32), we obtain the fraction of escape events along the relative position line.

This measured fraction, and the simulated fraction in Figure 38 b), are compared in Figure 41. The two fractions have their closest agreement between relative position 0.4 and 0.6. For lower relative positions, the measured fraction encounters background events, which are not included in the simulation. For the higher relative fraction, it becomes apparent that the measured proton peak is broader than what the simulation suggests.

The reliability of the escape event correction factor depends on how well the two fractions in Figure 41 agree. In this example, the method suggests a PSD selection that cuts at a relative position between 0.4 and 0.6.

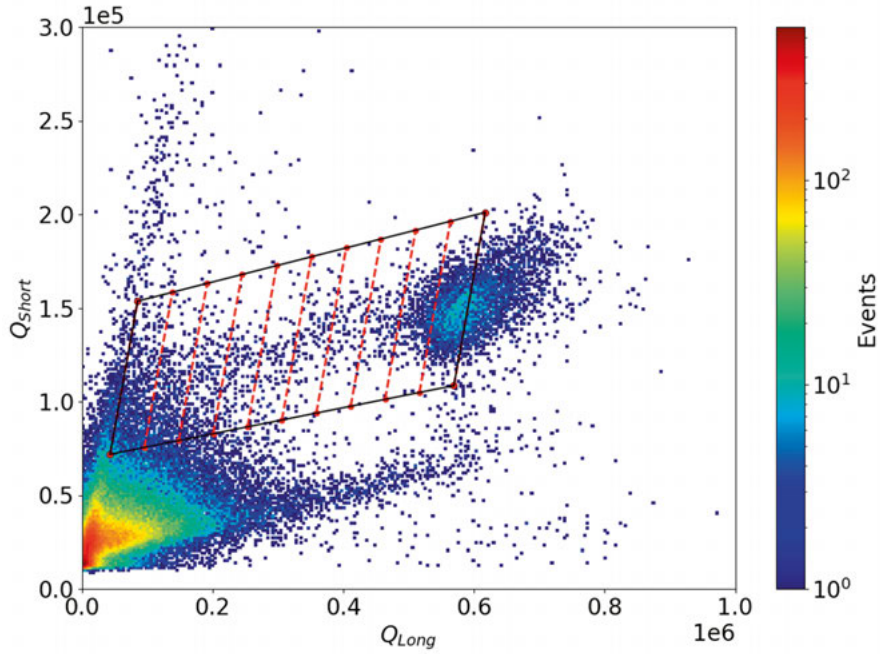


Figure 40: 2D histogram showcasing the binning made to estimate the number of escape events.

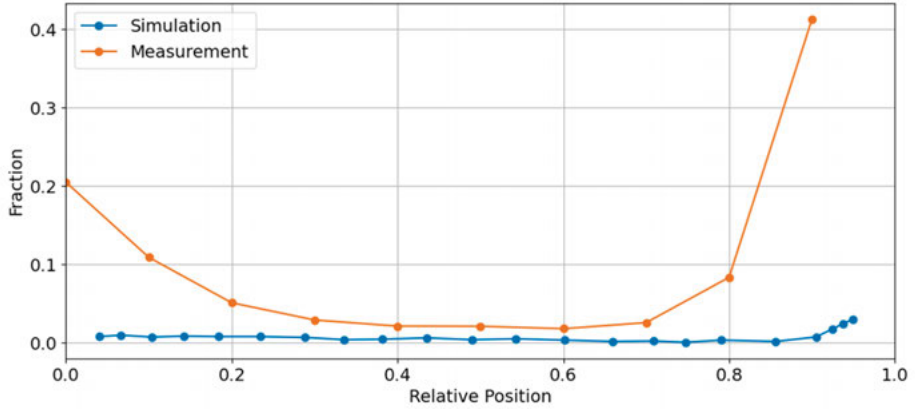


Figure 41: The simulated and measured fraction of escape events in the MPRU hodoscope, at positions relative to the proton peak.

4.4 Modelling and Analysis

This section gives an overview of the modelling used in the MPRu analysis. A detailed description of all steps taken is found in Paper III.

4.4.1 Neutron Spectrum Modelling

With the goal of estimating the thermonuclear emission, the model of the neutron spectrum is separated into contributions from thermonuclear and supra-thermal emission. This is achieved by modelling the velocity distributions of D and T fuel ions. In Paper III, we consider a Maxwellian distribution for the thermal bulk deuterons, a Maxwellian distribution for the thermal bulk tritons, and a supra-thermal distribution of deuterons due to auxiliary heating (NBI and RF). These distributions are modelled with the TRANSP code, with the following simplifications.

1. The ion temperature was set to be equal to the electron temperature.
2. The DT density fraction was not (as it often can be) used to determine the quality of the simulation.
3. The RF kick operator was not included, which means that the effect of RF is not simulated.

The first two simplifications do not affect the shape of the slowing-down distribution of the NBI ions, which is what we are primarily interested in obtaining from the TRANSP simulation. The last simplification is discussed in section 4.6.1 Charge Exchange Comparison.

The shape of the neutron emission spectrum can be described by different components based on their origin: we call the component from fusion reactions between two thermal bulk ions the thermal-thermal component. Similarly, fusion reactions between a thermal bulk ion and a supra-thermal ion contribute to the beam-thermal component. The spectral shapes of these components can be calculated with the DRESS code [50].

The MPRu system response matrix, see section 2.4.2 Examples, is applied to the thermal-thermal and beam-thermal spectral components. This converts the neutron spectra to simulated neutron counts in the hodoscope channels. Examples of the spectral components are showcased in Figure 42 a) before, and in Figure 42 b) after, the application of the system response matrix. The calculated spectral components are normalized, and their intensities I_{TH} and I_{BT} are used as fitting parameters in section 4.4.2 Neutron Spectrum Fit.

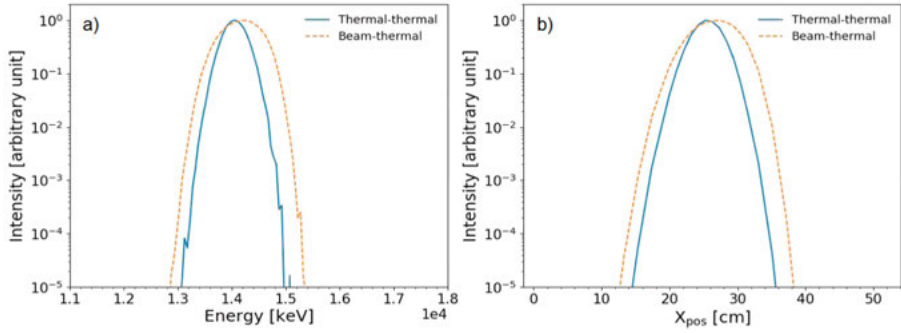


Figure 42: Normalized thermal-thermal and beam-thermal neutron spectral components. Shown as a function of energy in (a) and as a function of hodoscope position in (b) after the application of the system response matrix.

The effect of plasma rotation is not included in the TRANSP simulations. Instead, it is applied on the spectral components as an energy shift dE_{rot} , defined as

$$dE_{rot} = 0.54v_{rot} \cos \alpha, \quad (4.2)$$

where v_{rot} is the plasma rotation speed and α is the angle between the direction of rotation and the detector line of sight [60]. The angle α is set to 47° , a representative value for the MPRu LOS in the plasma, where most of the neutron emission comes from. The energy shift is used as a fitting parameter in section 4.4.2 Neutron Spectrum Fit.

This energy shift applies fully to the thermal-thermal component, where both reactants come from the rotating bulk plasma. For the beam-thermal component, only the thermal ion experiences this rotation. As an approximation, the energy shift on the beam-thermal component is set to $dE_{rot}/2$.

4.4.2 Neutron Spectrum Fit

The hodoscope spectral components are fit to match the measured hodoscope histogram in section 4.2 Measurement Data by minimizing the χ^2 test statistic. The fitting parameters consist of the energy shift dE_{rot} , and the intensities I_{TH} and I_{BT} of the thermal-thermal and beam-thermal components respectively. An example of a completed fit from Paper III is shown in Figure 43 a), with the state of the plasma discharge being shown in Figure 43 b) for the measured time interval.

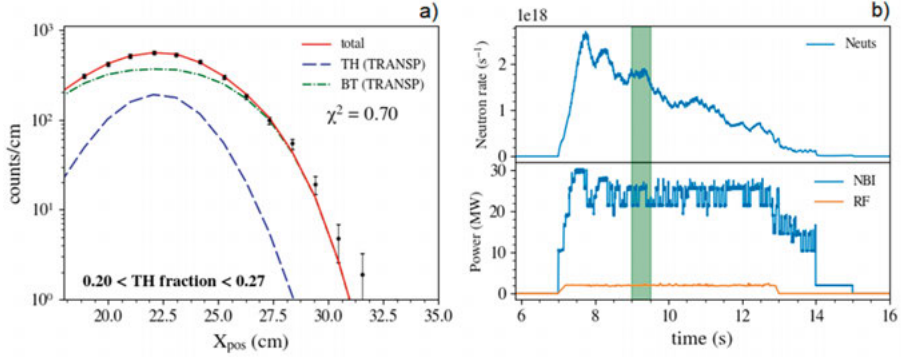


Figure 43: In (a) is a completed fit of the hodoscope histogram for the thermal-thermal (TH) and beam-thermal (BT) component, to the measured hodoscope histogram in black markers. In (b) is an overview of the neutron rate (estimated by the JET fission chambers), top panel, and the auxiliary heating power, bottom panel, with the time interval highlighted in green.

4.5 Results

4.5.1 Plasma Rotation

The plasma rotation v_{rot} speed is calculated from the fitted energy shift dE_{rot} using Equation 4.2. We can then express the plasma rotation as an angular frequency f_A in units of [rad/s], by dividing with the major radius. The MPRu LOS is dominated by the plasma core. As a result, we approximate the calculated angular frequency as the on-axis rotation using

$$f_A = \frac{v_{rot}}{R_0}, \quad (4.3)$$

where $R_0 \approx 3$ m is an approximation of the major radius in the core.

The plasma rotation estimates are compared to corresponding estimates from charge exchange [61]. In Figure 44 is a comparison over the normalized minor radius, with charge exchange estimates outside the core and the MPRu estimate as the on-axis rotation. The charge exchange estimate closest to the core is shown in a time trace with the MPRu estimate in Figure 45.

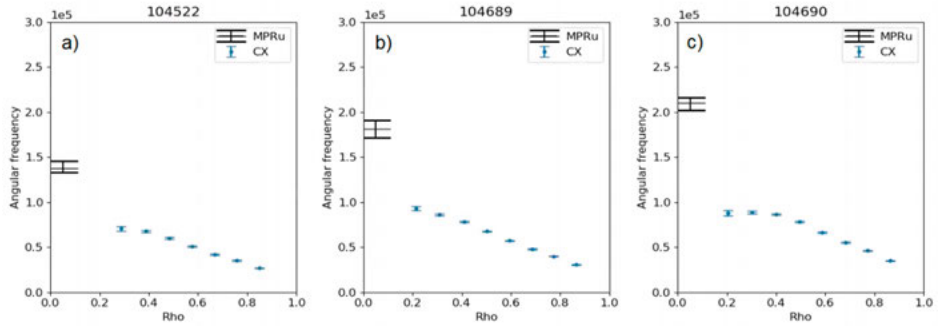


Figure 44: Plasma rotation, estimated by the MPRu and charge exchange spectroscopy for JET plasma discharges 104522 (a), 104689 (b), and 104690 (c). Rho denotes the normalized minor radius up to the last closed flux surface.

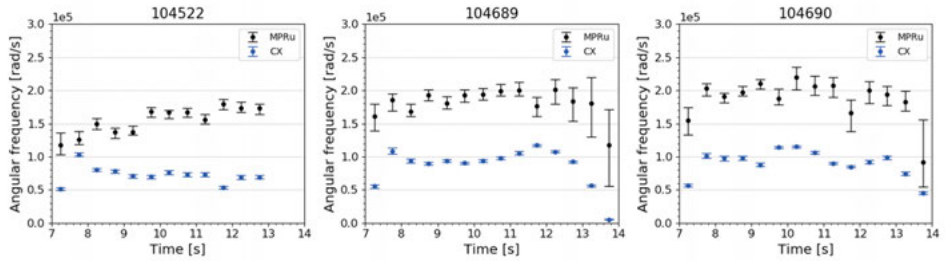


Figure 45: Time traces of the plasma rotation, estimated by the MPRu and charge exchange spectroscopy for JET plasma discharges 104522 (a), 104689 (b), and 104690 (c).

4.5.2 Thermonuclear Emission

The thermonuclear emission is expressed as a thermal fraction, calculated from spectral component intensities as

$$Thermal\ fraction = \frac{I_{TH}}{I_{TH} + I_{BT}}. \quad (4.4)$$

Time traces of the thermal fraction estimates for three of the analysed JET plasma discharges are shown in Figure 46.

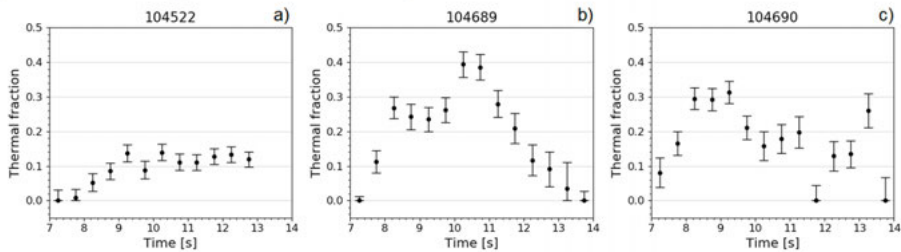


Figure 46: Time traces of the estimated thermal fraction for JET plasma discharges 104522 (a), 104689 (b), and 104690 (c).

4.6 Reflections on Paper III

4.6.1 Charge Exchange Comparison

While the charge exchange estimates of the plasma rotation in Figure 44 do not extend to the core, a linear projection suggests that the MPRu estimates are considerably higher. There is also a consistent disagreement from the time traces in Figure 45, though the reason for this is not fully understood.

For one JET plasma discharge, the RF kick operator was enabled in a TRANS simulation to investigate if the TRANSP model without the kick operator was overly simplified. The plasma rotation estimate with the simplified TRANSP model was on average 21% higher than the estimate with TRANSP simulating RF. Though this is a significant change, it is far from enough to explain the discrepancy between the MPRu and charge exchange estimates.

It is possible that data reduction techniques such as the escape event correction in section 4.3.2 Escape Event Correction will have an impact on the MPRu estimate. The correction would be applied to all channels and somewhat change the shape of the hodoscope histogram. It is unclear without testing, whether the resulting fit would yield a larger or smaller plasma rotation from this change.

4.6.2 Data Reduction

There are several opportunities for improvement in the data reduction codes of the MPRu. The escape event correction in section 4.3.2 Escape Event Correction in should ultimately provide a more accurate hodoscope histogram. One lightly explored subject is a background estimation. The higher hodoscope channels have very faint proton peaks, which makes them difficult to distinguish from background events when applying a PSD selection. This is troublesome since many features of interest, such as alpha knock-on [54], can be observed in the higher channels. An estimate of the number of background events, relative to the total neutron yield of a JET plasma discharge, could allow for either background subtraction in the PSD selection, or a background component in the hodoscope histogram.

4.6.3 Outlook

Paper III lays out the framework for estimating the plasma rotation and the thermonuclear emission with MPRu data. The state of the plasma rotation is discussed above, see section 4.6.1 Charge Exchange Comparison, but the thermal fraction estimate functions well on its own. It has not yet been compared to an equivalent measurement from another diagnostic, but that could be the

subject of future work. It could also be possible to perform comparisons with TRANSP simulations.

Regardless, the method for these estimate shows promise. It could be used to complement other diagnostics that have trouble penetrating into the core.

5. Conclusions

The primary accomplishment of this thesis has been the development of methods and codes to utilize full digital data acquisition systems. Both the JET neutron camera and the MPRu neutron spectrometer at JET have had upgrades to digital data acquisition systems. Until now, we have not been able to capitalize on these upgrades. A majority of my time has been spent on the development and testing of new data reduction and analysis codes for these systems. These codes are capable of expedient pulse processing and pile-up identification, pulse shape discrimination, and light yield calibration. Included are also graphical tools to aid the analysis, and necessary models and simulations. This enabled the development of methods for estimating the volume integrated neutron yield using the JET neutron camera, and the plasma rotation and thermonuclear emission using the MPRu. Both methods use measurement data and models for the respective instruments.

The neutron yield estimate uses a first principle physics method, and the latest method in Paper II absolutely calibrates the JET neutron camera. A large part of the work was put into the development of the system response matrix, and how it interfaces with the other models used for the neutron camera. The neutron yield estimates were compared with corresponding estimates by the JET fission chambers. In Paper I, the inconsistencies between the two systems was in line with expectations. Though the much larger inconsistencies in Paper II prompts further investigation.

The presented estimation methods for the MPRu show great promise, but the plasma rotation estimate needs to be studied further. Future work could expand the analysis to include comparisons with other JET diagnostics.

The developed data reduction codes still have many avenues to explore, which could improve the respective estimation methods. One particular concern for the neutron camera is the downshift of the light yield spectrum during high neutron rates. This effect should be investigated to either create some sort of correction, or somehow include the shift in the modelling. For the MPRu, both escape event correction and background estimation are features that could be developed further.

6. Summary in Swedish

Kärnfusion har länge varit en eftertraktad energikälla. Den lovar otroliga mängder fossilfri energi från relativt lite bränsle, skapat på ett säkert och hållbart vis. Men vägen till fusionsreaktorer är lång och har pågått i över 60 år, genom små och stora experiment och forskningskampanjer.

Kärnfusion grundar sig i att två atomkärnor slås samman i en så kallad fusionsreaktion. Tillsammans bildar de en atomkärna vars massa är mindre än den totala massan för de två ursprungliga atomkärnorna. Skillnaden i massa frigörs som energi enligt den välkända formeln $E = mc^2$. Mest energi frigörs från fusionsreaktioner mellan lätta atomkärnor. Av denna anledning är det tänkt att använda väteisotoperna deuterium (D) och tritium (T) som bränsle i fusionsreaktorer. Fusion av dessa två skapar en heliumatom och en neutron.

Sannolikheten för att fusionsreaktioner ska ske är starkt relaterat till bränslets temperatur. För en tillräcklig reaktionsrat krävs temperaturer omkring 100 miljoner Kelvin. Vid dessa temperaturer joniseras bränsleatomerna och bildar en sorts gas av atomkärnor och elektroner, detta tillstånd kallas för ett plasma. I en fusionsreaktor behöver detta plasma inneslutas så att fusionsreaktioner kan fortgå obehindrat.

Magnetisk inneslutning är en av de tekniker som används för att innesluta ett fusionsplasma. Tekniken har använts på forskningsanläggningar i årtionden och är aktuellt även för framtida projekt. Elektronerna och jonerna i ett plasma är laddade, och kommer därför följa fältlinjerna i ett magnetiskt fält. Ett plasma kan inneslutas genom att konstruera ett magnetiskt fält där fältlinjerna bildar en sluten cirkel. Denna teknik används i det reaktorkoncept som kallas för en "tokamak", vilket utvecklades i Sovjetunionen under 1960-talet. Det största tokamakexperimentet i världen är JET (Joint European Torus) i Oxfordshire, Storbritannien. Metoderna som beskrivs i denna avhandling har utvecklats för två olika mätinstrument på JET.

Neutroner från fusionsreaktioner har en neutral laddning, och påverkas därmed inte av magnetfältet. Ett fusionsplasma utsöndrar både neutroner och fotoner. Genom att mäta antalet, energifördelningen, och ursprungspositionen i plasmat för neutronerna och fotonerna så kan vi uppskatta olika sorters plasmaegenskaper. En forskningsanläggning som JET har en stor uppsättning mätinstrument för denna typ av mätningar.

Den här avhandlingen fokuserar på metoder för att mäta neutroner med hjälp av scintillatorer, en detektortyp som skapar en ljussignal när en partikel

interagerar med scintillatormaterialet. Avhandlingen följer förloppet från att en partikel träffar detektorn och skapar en ljussignal, till hur de uppmätta signalerna behandlas och analyseras. En ljussignals pulsform och storlek bär information om vilken sorts partikel som uppmättes, och hur mycket energi den deponerade i detektorn. För neutroner är länken mellan neutronenergi och uppmätt energi inte uppenbar, och kräver därför specifika modeller och simuleringar för att fullborda analysen. En stor del av arbetet har varit att utveckla datareduktionskoder, analyskoder, och modeller för att utföra dessa steg för två olika mätinstrument på JET; neutronkameran och den uppgraderade magnetiska protonrekylspektrometern (MPRu).

Neutronkameran används för att övervaka en tvådimensionell profil av fusionsplasmats neutronemission. Den består av 19 siktlinjer med två typer av scintillatordetektorer i varje siktlinje. I det här arbetet har vi utvecklat en metod för att uppskatta den volymintegrerade neutronraten med hjälp av neutronkameran. Neutronraten kan direkt kopplas till fusionsraten, vilket är ett mått på vilken effekt som uppnås i en reaktor. Metoden använder mätdata från neutronkameran. Samt modeller för detektorernas egenskaper, kamerans geometri, och neutronemissionen från fusionsplasmats. Med hjälp av modellerna och transportkoder kan vi simulera neutroner som färdas från fusionsplasmats och inducerar ljuspulser i kamerans scintillatorer. Vi jämför de simulerade och uppmätta signalerna, och justerar modellen av neutronemissionen i en anpassning tills jämförelsen stämmer bra överens. På så vis fås en modell av neutronemissionen som är understödd av neutronkamerans mätdata. Från modellen kan vi sedan uppskatta den volymintegrerade neutronraten.

Uppskattningen av neutronraten gjordes i två iterationer för neutronkameran, där de två olika scintillatortyperna i kameran användes i två olika experimentkampanjer (DTE2 och DTE3). Båda dessa jämfördes med liknande uppskattningar av neutronraten från ett annat mätinstrument på JET, fissionskamrarna. Överensstämmelsen mellan uppskattningarna visade sig vara bristfällig, och skilde sig även kraftigt mellan de två iterationerna. Detta uppmanar till ytterligare studier och utveckling av metoden med neutronkameran.

MPRu kan mäta neutronenergi med hög energiupplösning. Avhandlingen beskriver ett ramverk för att uppskatta två olika egenskaper för fusionsplasmats; plasmarotationen och den termiska neutronemissionen. På grund av den siktlinje som MPRu har, så uppskattas dessa egenskaper i centrum av plasmats. Ramverket visar sig vara mycket lovande, och uppskattningarna från metoden kan potentiellt komplettera andra uppskattningar av samma egenskaper. Detta skulle främst stödja de mätinstrument som har svårt att göra mätningar och uppskattningar i centrum av plasmats.

De modeller, tekniker och koder som presenteras i avhandlingen har stor utvecklingspotential, och kan potentiellt användas till liknande mätinstrument.

7. Acknowledgements

I want to begin by thanking my main supervisor, Erik. You have been a fantastic guide throughout this journey. You have taught me so many things from programming to plasma physics. But most importantly, you have been someone I could always turn to with questions. Thank you for your patience and compassion.

I also want to thank Göran and Sean, my other supervisors. Sean, thank you for all you have taught me in MCNP and Python, for your insights into all things JET and tokamaks, and for just stopping by to chat sometimes. Göran, thank you for your guidance throughout the project, for your keen comments on my writing, and for the trust you placed in me to co-supervise a master student. Your enthusiasm for the MPRu is infectious.

Thank you to my office mate Benjamin and the other past PhD students, Andrea, Arne, Benjaminas, for helping me on this journey. Thank you to Jila for the fun talks we had.

Thank you to Jacob for your support with the MPRu work, your writing tips, and for sharing your insights in plasma physics. Thank you to Matthias for your help with the NESSA2.5 project, I'm sure we will finish it eventually. Thank you to Mattias for the fun times at SciFest and for helping out with the TRIGA lab in Ljubjana. Thank you to Anders for your lovely company, I enjoyed the teaching we did together. Thank you to Marco for your support as my supervisor for my master diploma work, which led me to the fusion group soon after. Thank you to the rest of the TK members.

Finally, I want to thank my family for their loving support and their constant reminders for me not to push myself too hard.

Bibliography

- [1] L. A. Artsimovich, “Tokamak devices” *Nuclear Fusion*, vol. 12, pp. 215-252
- [2] F.F Chen, ”Plasma Applications”, in *Introduction to Plasma Physics and Controlled Fusion*, pp. 355-411, Cham: Springer International Publishing (2016).
- [3] EUROfusion “JET”, available at <https://euro-fusion.org/devices/jet/> [from 2024-12-19].
- [4] Princeton Plasma Physics Laboratory “Tokamak Fusion Test Reactor”, available at <https://www.pppl.gov/tokamak-fusion-test-reactor> [from 2024-12-19].
- [5] JT-60SA “What is JT60SA?”, available at <https://www.jt60sa.org/wp/> [from 2024-12-19].
- [6] ITER “ITER Overview”, available at <https://www.iter.org/few-lines> [from 2024-12-19].
- [7] INTERNATIONAL ATOMIC ENERGY AGENCY, *Fusion Physics, Non-serial Publications*, IAEA, Vienna (2012).
- [8] J. Frenje, et al., “Neutron emission Doppler-shift measurements in deuterium-tritium plasmas”, *Rev. Sci. Instrum.* 70, 1176-1180 (1999).
- [9] B. Lehnert, ”Rotating Plasmas”, *Nucl. Fusion* 11 485 (1971).
- [10] G. F. Knoll, *Radiation Detection and Measurement* (John Wiley & Sons, Inc., 2000).
- [11] Eljen Technology “Neutron / Gamma PSD EJ-301, EJ-309”, available at <https://eljentechnology.com/products/liquid-scintillators/ej-301-ej-309> [from Dec 17 2024].
- [12] Eljen Technology “Fast Timing EJ-228, EJ-230”, available at <https://eljentechnology.com/products/plastic-scintillators/ej-228-ej-230> [from Dec 17 2024].
- [13] A. G. Wright, *The Photomultiplier Handbook* (Oxford University Press, 2017).
- [14] Teledyne SP Devices “Pulse Detection (FWPD), available at <https://www.spdevices.com/what-we-do/products/firmware/fwfpd> [from Dec 17 2024].
- [15] E. Andersson Sundén, et al., “The thin-foil magnetic proton recoil neutron spectrometer MPRu at JET”, *Nuclear Instruments and Methods in Physics Research A* 610 (2009) 682–699.

- [16] J. Zhou, et al., “Generalized method for the optimization of pulse shape discrimination parameters”, Nuclear Inst. And Methods in Physics Research, A 1050 (2023) 168184.
- [17] SciPy “scipy.signal.find_peaks”, available at https://docs.scipy.org/doc/scipy/reference/generated/scipy.signal.find_peaks.html [Dec 17 2024]
- [18] M. Preston, et al., “A feature-extraction and pile-up reconstruction algorithm for the forward-spectrometer EMC of the PANDA experiment”, Nucl Inst. and Methods in Physics Research, A 1011 (2021) 165601.
- [19] A. Sahlberg, et al, “Forward modeling of pile-up events in liquid scintillator detectors for neutron emission spectroscopy”, Rev. Sci. Instrum. 92, 083502 (2021).
- [20] M. Riva, et al., “Hardware architecture of the data acquisition and processing system for the JET Neutron Camera Upgrade (NCU) project”, Fusion Engineering and Design 123 (2017) 873-876.
- [21] L. Ballabio, et al., ”Relativistic Calculation of Fusion Product Spectra for Thermonuclear Plasmas”, Nucl. Fusion 38 1723 (1998).
- [22] S. Conroy, Uppsala University, private communication (2023).
- [23] MCNP® USER’S MANUAL Code Version 6.2, section 3.3.5.18
- [24] W. Cash, “Parameter estimation in astronomy through application of the likelihood ratio,” Astrophys. J. 228, 939–947 (1979).
- [25] H. Brysk “Fusion Neutron Energies and Spectra”, Plasma Physics, Vol. 15, pp. 611 to 617 (1973)
- [26] P. Van Belle and G. Sadler, “The computation of fusion product spectra from high temperature plasmas,” Proceedings of the Course Workshop on Basic and Advanced Techniques for Fusion Plasmas, Varenna 3, 767 (1986).
- [27] D. Schmidt, et al., “Characterization of liquid scintillator detectors”, Nuclear Instruments and Methods in Physics Research A 476 (2002) 186-189.
- [28] N. Mauritzson, et al., “Light-yield response of liquid scintillators using 2-6 MeV tagged neutrons”, Nuclear Instruments and Methods in Physics Research A 1062 (2024) 169197.
- [29] J. Scherzinger, et al., ”The light-yield response of a NE-213 liquid-scintillator detector measured using 2–6 MeV tagged neutrons”, Nuclear Instruments and Methods in Physics Research A 840 (2016) 121-127.
- [30] K. Gul, et al., “Relative neutron detector efficiency and response function measurements with A 252Cf neutron source”, Nuclear Instruments and Methods in Physics Research A278 (1989) 470-476.
- [31] E. Dekempeneer, et al., ”A spectrometer for double-differential neutron-emission cross section measurements in the energy range 1.6 to 16 MeV”, Nuclear Instruments and Methods in Physics Research A256 (1987) 489-498.

- [32] W.W. Lindstrom, B. Anderson, "Improved Computer Simulation of the Detection Process in NE-102 and NE-213 Scintillators for 0 to 4.8 MeV Neutrons", *Nuclear Instruments and Methods* 98 (1972) 413-417.
- [33] N.P. Hawkes, et al., "The design of a proton recoil telescope for 14 MeV neutron spectrometry", *Nuclear Instruments and Methods in Physics Research A* 476 (2002) 506-510.
- [34] B. Marcinkevicius, et al., "A Thin-foil Proton Recoil spectrometer for DT neutrons using annular silicon detectors", *JINST* 14 P03007 (2019).
- [35] D. B. Syme, et al., "Fusion yield measurements on JET and their calibration," *Nucl. Eng. Des.* 246, 185–190 (2012).
- [36] P. Batistoni, et al., "14 MeV calibration of JET neutron detectors - phase 2: in-vessel calibration" *Nucl. Fusion* 58 106016 (2018).
- [37] O. N. Jarvis, "Neutron measurement techniques for tokamak plasmas" *Plasma Physics and Controlled Fusion* 36, 209 (1994).
- [38] B. Esposito, et al., "Ohmic ion temperature and thermal diffusivity profiles from the JET neutron emission profile monitor" *Plasma Physics and Controlled Fusion* 35, 1433-1440 (1993).
- [39] J. Eriksson, et al., "Deuterium density profile determination at JET using a neutron camera and a neutron spectrometer" *Review of scientific instruments* 85, 11E106 (2014).
- [40] F. Binda, et al., "Forward fitting of experimental data from a NE213 neutron detector installed with the magnetic proton recoil upgraded spectrometer at JET" *Review of Scientific Instruments* 85, 11E123 (2014).
- [41] S. Popovichev, et al., "Performance of neutron measurements during trace tritium experiments on JET" *Proceedings of the 31st EPS Conference on Plasma Phys. London, UK, ECA 28G* (2004).
- [42] D. Marocco, et al., "Exploration of ion temperature profile measurements at JET using the upgraded neutron profile monitor" *Review of Scientific Instruments* 83, 10D314 (2012).
- [43] The EUROfusion internal Figure Database, available at <https://figures.jetdata.eu> [from May 31, 2022].
- [44] NumPy "numpy.lib.stride_tricks.as_strided", available at https://numpy.org/doc/stable/reference/generated/numpy.lib.stride_tricks.as_strided.html [from Dec 17 2024].
- [45] F. Binda, et al., "Calculation of the profile-dependent neutron backscatter matrix for the JET neutron camera system", *Fusion Engineering and Design* 123, 865-868 (2017).
- [46] L. C. Appel, et al., "A unified approach to equilibrium reconstruction," in 2006 33rd EPS Conference on Plasma Physics, Rome (European Physical Society, 2006), p. P2.184.

- [47] E. Ronchi, et al., “A parametric model for fusion neutron emissivity tomography for the KN3 neutron camera at JET”, Nuclear Fusion (2010).
- [48] C. Hellesen, et al., “Validating TRANSP simulations using neutron emission spectroscopy with dual sight lines” Review of scientific instruments 79 (2008).
- [49] P. Sirén, et al., ”Synthetic neutron camera and spectrometer in JET based on AFSI-ASCOT simulations”, JINST 12 C09010 (2017)
- [50] J. Eriksson, et al., “Calculating fusion neutron energy spectra from arbitrary reactant distributions”, Computer Physics Communications 199 (2016) 40-46.
- [51] D. Foreman Mackey, et al., “emcee: The MCMC Hammer”, Publications of the Astronomical Society of the Pacific 125 (925) (2013) 306.
- [52] J. Garcia, “Deuterium-tritium experiments in JET with the ITER-like wall”, TTF 2022 - US-EU Joint Transport Taskforce Workshop, Apr 2022, Santa Rosa (CA), United States. Cea-03659111.
- [53] Eurofusion “Breaking New Ground: JET Tokamak’s Latest Fusion Energy Record Shows Mastery of Fusion Processes”, available at <https://euro-fusion.org/eurofusion-news/dte3record/> [from Apr 12 2024]
- [54] J. Källne, et al., ”Observation of the Alpha Particle ‘Knock-On’ Neutron Emission from Magnetically Confined DT Fusion Plasmas”, Phys. Rev. Lett. (2000) 1246.
- [55] J. Eriksson, et al., ”Calculation of α knock-on neutron spectra from JET DT plasmas”, 49th EPS Conference on Contr. Fusion and Plasma Phys, 3-7 July 2023.
- [56] H. Henriksson, et al., ”Systematic spectral features in the neutron emission from NB heated JET DT plasmas”, Plasma Phys. Control. Fusion 47 (2005) 1763.
- [57] H. Henriksson, et al., ”Synergetic RF and NB heating effects in JET DT plasmas studied with neutron emission spectroscopy”, Nucl. Fusion 46 (2006) 244.
- [58] J. Frenje, et al., “Neutron emission Doppler-shift measurements in deuterium–tritium plasmas”, Rev. Sci. Instrum. 70, 1176-1180 (1999).
- [59] G. Wikström 2005 “Performance studies of phoswich detectors in the upgraded Magnetic Proton Recoil neutron spectrometer” Uppsala University Neutron Physics Report 05#01
- [60] G. Gorini, et al., ”Neutron spectrometry for plasma rotation”, Review of scientific instruments 68, 561-564 (1997).
- [61] M. G. von Hellermann, et al., ”Visible charge exchange spectroscopy at JET”, Rev. Sci. Instrum. 61, 3479-3486 (1990).

Acta Universitatis Upsaliensis

Digital Comprehensive Summaries of Uppsala Dissertations from the Faculty of Science and Technology 2491

Editor: The Dean of the Faculty of Science and Technology

A doctoral dissertation from the Faculty of Science and Technology, Uppsala University, is usually a summary of a number of papers. A few copies of the complete dissertation are kept at major Swedish research libraries, while the summary alone is distributed internationally through the series Digital Comprehensive Summaries of Uppsala Dissertations from the Faculty of Science and Technology. (Prior to January, 2005, the series was published under the title “Comprehensive Summaries of Uppsala Dissertations from the Faculty of Science and Technology”.)

Distribution: publications.uu.se
urn:nbn:se:uu:diva-545704



ACTA UNIVERSITATIS
UPSALIENSIS
2025